

Detailed Studies of a High-Capacity Electrode Material for Rechargeable Batteries, $\text{Li}_2\text{MnO}_3 - \text{LiCo}_{1/3}\text{Ni}_{1/3}\text{Mn}_{1/3}\text{O}_2$

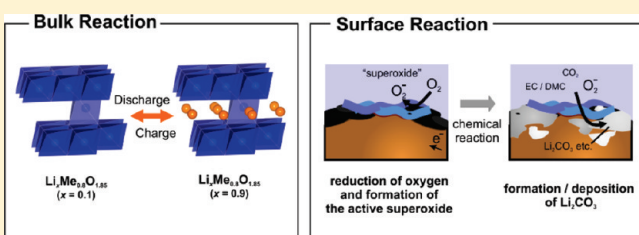
Naoaki Yabuuchi,[†] Kazuhiro Yoshii,[†] Seung-Taek Myung,[‡] Izumi Nakai,[†] and Shinichi Komaba^{*,†}

[†]Department of Applied Chemistry, Tokyo University of Science, 1-3 Kagurazaka, Shinjuku, Tokyo 162-8601, Japan

[‡]Department of Chemical Engineering, Iwate University, Morioka, Iwate 020-8551, Japan

Supporting Information

ABSTRACT: Lithium-excess manganese layered oxides, which are commonly described by the chemical formula $z\text{Li}_2\text{MnO}_3 - (1-z)\text{LiMeO}_2$ (Me = Co, Ni, Mn, etc.), are of great importance as positive electrode materials for rechargeable lithium batteries. In this Article, $\text{Li}_x\text{Co}_{0.13}\text{Ni}_{0.13}\text{Mn}_{0.54}\text{O}_2 - \delta$ samples are prepared from $\text{Li}_{1.2}\text{Ni}_{0.13}\text{Co}_{0.13}\text{Mn}_{0.54}\text{O}_2$ (or $0.5\text{Li}_2\text{MnO}_3 - 0.5\text{LiCo}_{1/3}\text{Ni}_{1/3}\text{Mn}_{1/3}\text{O}_2$) by an electrochemical oxidation/reduction process in an electrochemical cell to study a reaction mechanism in detail before and after charging across a voltage plateau at 4.5 V vs Li/Li⁺. Changes of the bulk and surface structures are examined by synchrotron X-ray diffraction (SXRD), X-ray absorption spectroscopy (XAS), X-ray photoelectron spectroscopy (XPS), and time-of-flight secondary ion mass spectroscopy (SIMS). SXRD data show that simultaneous oxygen and lithium removal at the voltage plateau upon initial charge causes the structural rearrangement, including a cation migration process from metal to lithium layers, which is also supported by XAS. This is consistent with the mechanism proposed in the literature related to the Li-excess manganese layered oxides. Oxygen removal associated with the initial charge on the high voltage plateau causes oxygen molecule generation in the electrochemical cells. The oxygen molecules in the cell are electrochemically reduced in the subsequent discharge below 3.0 V, leading to the extra capacity. Surface analysis confirms the formation of the oxygen containing species, such as lithium carbonate, which accumulates on the electrode surface. The oxygen containing species are electrochemically decomposed upon second charge above 4.0 V. The results suggest that, in addition to the conventional transition metal redox reactions, at least some of the reversible capacity for the Li-excess manganese layered oxides originates from the electrochemical redox reaction of the oxygen molecules at the electrode surface.



INTRODUCTION

The demand for the large-scale rechargeable batteries has grown rapidly over the past few years. In the realm of energy storage, lithium-ion batteries are of great significance as power sources to realize cleaner and energy-efficient automobiles, that is, pure electric vehicles. The elemental abundance in earth's crust is the most important factor to design the electrode materials for large-scale applications. For this purpose, the iron- and manganese-based materials are promising candidates as the positive electrode materials. Two possible candidates, LiMn_2O_4 (and its derivatives) and LiFePO_4 , are used as the positive electrode materials for the large-scale application. Much fundamental research progress in both materials has been achieved in the past two decades.^{1–10} However, available rechargeable capacity for both materials approaches almost the theoretical limit, indicating that alternative positive electrode materials achieving higher energy density than that of LiMn_2O_4 and LiFePO_4 are needed to meet the demand for further enhancement of the energy density of the rechargeable batteries.

Among the positive electrode materials reported so far, Li-excess manganese layered oxides represented by the chemical formula $z\text{Li}_2\text{MnO}_3 - (1-z)\text{LiMeO}_2$ (Me = Co, Ni, Mn, etc.) seem to be among of the most promising candidates and can

deliver higher capacity ($>230 \text{ mAh g}^{-1}$) with higher operating voltage ($>3.5 \text{ V}$ vs Li/Li⁺ in average). A characteristic feature of the Li-excess manganese layered oxides is a voltage plateau observed at 4.5–4.6 V during an initial cycle. Their electrode performance is drastically improved by charging across the voltage plateau. However, a large irreversible capacity in this process is often observed. The larger polarization and continuous structural transition also makes it more difficult to develop this material as a positive electrode material for the rechargeable lithium batteries.

To utilize the Li-excess manganese layered oxides as the electrode materials, they have been extensively studied over the past several years. The structural compatibility between LiMeO_2 (Me; 3d-transition metals, such as Co, Ni, and Mn) and Li_2MnO_3 (alternatively designated as $\text{Li}[\text{Li}_{1/3}\text{Mn}_{2/3}] \text{O}_2$ in a layered formulation) as layered rock-salt structures allows for their structural integration, and these materials can be denoted as $z\text{Li}_2\text{MnO}_3 - (1-z)\text{LiMeO}_2$ as proposed by Thackeray and co-workers.^{11–14} The Li-excess manganese layered oxides are also simply reformulated as $\text{Li}[\text{Li}_{x/3}\text{Me}_{1-x}\text{Mn}_{2x/3}]$ ($0 < x < 1$). Several individual groups have examined different systems, for example, LiCoO_2 ,¹⁵

Received: September 23, 2010

Published: March 04, 2011

LiCrO_2 ,¹⁶ and $\text{LiNi}_{1/2}\text{Mn}_{1/2}\text{O}_2$.^{17–19} In the layered positive electrode materials, LiMeO_2 , it is generally accepted that the charging (oxidation of transition metals associated with a lithium extraction process) is limited by the amount of the transition metal ions in the tetravalent state. The charging ends when all of the transition metals are oxidized to a tetravalent state. As a result, Li_2MnO_3 , consisting of Mn^{4+} only, was considered to be electrochemically inactive as an electrode material. However, Li-excess manganese layered oxides,^{11–14,17–29} even pure Li_2MnO_3 ,^{30–34} are indeed electrochemically active as the electrode materials. A significant amount of Li ions is extracted upon initial charge from these Li-excess manganese layered oxides accompanied by the well-defined voltage plateau at 4.5–4.6 V. The reaction mechanism associated with the voltage plateau also has been extensively studied. Lu and Dahn have proposed simultaneous Li^+ and O^{2-} removal at the plateau based on Rietveld analysis, forming oxygen vacancies in the crystal lattice.¹⁸ Robertson and Bruce have confirmed that Li^+/H^+ exchange occurs at the elevated temperatures (55 °C) based on the study on pure Li_2MnO_3 .^{31,32} The proton originated from the decomposition of the electrolyte solution, such as dimethyl carbonate (DMC) and ethylene carbonate (EC). Recently, this was directly supported by the detailed gas analysis by mass spectroscopy by the research group of SANYO.³⁴ In pure Li_2MnO_3 , CO_2 , which is a decomposition product of the electrolyte, becomes the dominant component at elevated temperature, while oxygen molecule released from the lattice is a prominent component at room temperature. A ^1H MAS NMR study on the Li-excess system $\text{Li}_{1.12}(\text{Ni}_{0.425}\text{Mn}_{0.425}\text{Co}_{0.15})_{0.88}\text{O}_2$ by Croguennec et al. also suggested that Li^+/H^+ exchange is minimal at room temperature.³⁵ The change in the crystal structure accompanied by the oxygen removal process has been examined by neutron diffraction combined with the in situ differential electrochemical mass spectrometry (DEMS).³⁶ A cation migration model was proposed as the oxygen removal process. Oxygen is first removed from the material surface, and then remaining transition metals migrate from the surface into the inside particles. Formation of the oxygen vacancy and its diffusion in the crystal lattice were not assumed in this model. Similarly, the “lattice densification” model has been proposed on the basis of the analytical results obtained by XRD.³⁵ The cation rearrangement process has been further supported by a ^6Li MAS NMR study.²²

Although the reaction mechanisms for the Li-excess manganese layered oxides have been extensively examined, the analytical techniques used in the most of those works are limited to the studies on the bulk of particles. Many questions are still unanswered, because little information is available on the surface composition of the Li-excess manganese layered oxides. One of the unanswered questions about the Li-excess manganese layered oxides is the specific role of the oxygen molecules that are released during initial charge at the voltage plateau in the electrochemical reactions for the subsequent cycles. This issue is first dealt with in this Article by applying surface analytical methods, and we address whether or not oxygen molecules may indeed participate in the electrochemical redox reactions. The theoretical capacity of the oxygen reaches 800 mAh g⁻¹ when the one-electron reduction reaction per an oxygen molecule is assumed. This is not negligible even if the small amount of oxygen exists in the cell. Surface analysis has been performed by X-ray photoelectron spectroscopy (XPS) combined with the secondary ion mass spectroscopy (SIMS). XPS spectra are collected by irradiating

a target with X-rays while the kinetic energy of escaped electrons from the top 1–10 nm of the target is analyzed. The binding energies of the escaped electrons have characteristic features for the elements in a certain chemical environment, which allow for a detailed examination of the atomic compositions of a target and the chemical and electronic states of a specific element. Recently, the application of XPS in analysis of the degradation mechanisms of the electrode materials related to surface structural changes has been described in the literature.^{37–40} Secondary ion mass spectroscopy (SIMS)^{41,42} is also utilized as a complementary surface analytical method to XPS, which is based on the mass spectrometric analysis on ions. For SIMS, primary ions, accelerated in the range of 10–20 keV, are bombarded to a target. A small fraction of the target is evaporated from the outer surface layer of the target as various different kinds of ionized molecular fragments. The ionized molecular fragments are counted using a time-of-flight (TOF) mass spectrometer. The mass of the fragments involves information on the chemical species formed on the electrode uppermost surface layers. In addition to the chemical state, the high spatial resolution of the SIMS provides a detailed two-dimensional map of the surface.

In this Article, a detailed study of the reaction mechanisms of the Li-excess manganese layered oxides in relation to the changes of both bulk and surface structures is presented. A one-to-one mixture between Li_2MnO_3 and $\text{LiCo}_{1/3}\text{Ni}_{1/3}\text{Mn}_{1/3}\text{O}_2$ ($\text{Li}_{1.2}\text{Co}_{0.13}\text{Ni}_{0.13}\text{Mn}_{0.54}\text{O}_2$) was chosen as a representative material of the Li-excess manganese layered oxides. $\text{LiCo}_{1/3}\text{Ni}_{1/3}\text{Mn}_{1/3}\text{O}_2$ is well established high-energy (over 200 mAh g⁻¹ is achieved) and high-power positive electrode material having an ideal layered structure,^{43–45} and the mixture with Li_2MnO_3 also can be found in the literature.^{14,23,26–28,46} This combined study on both bulk and surface analysis allows for a better understanding of the reaction mechanisms of the Li-excess manganese layered oxides before and after initial charging beyond the voltage plateau of 4.5–4.6 V.

■ EXPERIMENTAL SECTION

Sample Preparation. $0.5\text{Li}_2\text{MnO}_3-0.5\text{LiCo}_{1/3}\text{Ni}_{1/3}\text{Mn}_{1/3}\text{O}_2$ ($\text{Li}_{1.2}\text{Co}_{0.13}\text{Ni}_{0.13}\text{Mn}_{0.54}\text{O}_2$) was prepared by a solid-state reaction from lithium hydroxide and cobalt–nickel–manganese hydroxide ($\text{Co}, \text{Ni}, \text{Mn})(\text{OH})_2$). The cobalt–nickel–manganese hydroxide was prepared by a coprecipitation method from 2.0 mol dm⁻³ of $\text{Co}(\text{NO}_3)_2$, $\text{Ni}(\text{NO}_3)_2$, and $\text{Mn}(\text{NO}_3)_2$ ($\text{Co:Ni:Mn} = 0.13:0.13:0.54$ in the molar ratio) aqueous solution and 2.0 mol dm⁻³ of LiOH aqueous solution with the desired amount of NH_4OH . The solutions were mixed slowly in a nitrogen filled glovebag, and the pH of the mixed solution was kept in the range of 11–12 during the precipitation process. Finally, the precipitated ($\text{Co}, \text{Ni}, \text{Mn})(\text{OH})_2$ particles were filtered, washed by degassed water, and then dried in a vacuum at room temperature. Thus obtained ($\text{Co}, \text{Ni}, \text{Mn})(\text{OH})_2$ and LiOH were mixed in the molar ratio of 1.00:1.05 by using a mortar and pestle, and pressed into pellets, in which 5% of excess lithium was added to compensate for the lithium evaporation during the calcinations at high temperature. The pellets were heated at 900 °C for 10 h in air and then quenched to room temperature.

Electrochemical Testing. Composite positive electrodes consisted of 80 wt % active material, 10 wt % acetylene black, and 10 wt % polyvinylidene fluoride (PVdF), pasted on aluminum foil as a current collector. The electrolyte solution used was 1 mol dm⁻³ LiPF_6 dissolved in EC:DMC = 1:1 (Kishida Chem. Corp., Ltd., Japan). Electrochemical testing was conducted using R2032-type coin cells with Li metal as negative electrodes. The cells were assembled in an argon filled glovebox.

Electrochemical testing condition is specified in the Results and Discussion.

Synchrotron X-ray Diffraction (XRD) Analysis. Synchrotron X-ray diffraction patterns were collected at the beamline BL02B2, SPring-8 in Japan, equipped with a large Debye–Scherrer camera.⁴⁷ $\text{Li}_x\text{Co}_{0.13}\text{Ni}_{0.13}\text{Mn}_{0.54}\text{O}_{2-\delta}$ composite electrodes were electrochemically prepared in the coin cells at a rate of 10 mA g^{-1} and gently rinsed with dimethyl carbonate (DMC) to remove excess electrolyte from the composite electrode, and then were dried at room temperature in the argon filled glovebox. The composites were separated from the aluminum current collectors and cut into small pieces using a metallic blade, and then were filled into glass capillaries (1.0 mm diameter or 0.5 mm for the pristine powder). The glass capillaries were sealed by a resin in the argon filled glovebox to eliminate the sample exposure to air. To minimize the effect of X-ray absorption by the samples, the wavelength of incident X-ray beam was set to 0.5 Å using a silicon monochromator, which was calibrated to 0.5028(1) Å with a CeO_2 standard. X-ray diffraction data were recorded on an imaging plate for 20 min. Rietveld refinement analysis was carried out using RIETAN2000⁴⁸ in the 2θ range of 10 – 40° , corresponding to 31 to $>180^\circ$ for $\text{Cu K}\alpha$ radiation.

X-ray Absorption Spectroscopy (XAS). X-ray absorption spectroscopy was performed at the beamline BL-12C of the Photon Factory Synchrotron Source in Japan. XAS spectra were collected with a silicon monochromator in transmission mode. The intensity of incident and transmitted X-ray was measured by using an ionization chamber at room temperature. $\text{Li}_x\text{Co}_{0.13}\text{Ni}_{0.13}\text{Mn}_{0.54}\text{O}_2$ composite samples were prepared by using the coin cells at a current density of 10 mA g^{-1} . The composite electrodes were rinsed with DMC and sealed in a water-resistant polymer film in the argon filled glovebox. Analysis of the XAS spectra was carried out by using program code of IFEFFIT.⁴⁹ The postedge background was determined using a cubic spline procedure. The normalized EXAFS spectra were converted from energy to wavevector k , and then weighted by k^3 . EXAFS structural parameters were obtained by a nonlinear least-squares analysis of the data using phase shift and amplitude function generated from the FEFF code.⁵⁰ The least-squares curve fitting was carried out in R -space. Simulation of the XANES spectra was conducted by using the program code FEFF 8.0 with the cluster size of 6.0 \AA from the centered atoms, which typically consisted of 66 atoms.

X-ray Photoelectron Spectroscopy (XPS). XPS measurements were performed using an X-ray photoelectron spectrometer (JEOL, JPS-9010MC). XPS spectra were collected at room temperature using a nonmonochromatic $\text{Mg K}\alpha$ (1253 eV) X-ray source operated at 120 W (12 kV and 10 mA), and the chamber pressure was kept $<10^{-6}$ Torr during the measurements. The energy of the spectra was calibrated by the binding energy of the hydrocarbon ($\text{C}-\text{H}$) at 284.6 eV , which is mainly contributed by the acetylene black in the composite electrode.

Time-of-Flight-Secondary Ion Mass Spectroscopy (TOF-SIMS). TOF-SIMS measurements were performed by using a time-of-flight secondary ion mass spectrometer (TOF-SIMS, TFS2000, ULVAC-PHI Inc.), equipped with a liquid Ga ion source and pulse electron flooding. During analysis, the targets were bombarded by the 15 kV Ga beams with pulsed primary ion current varying from 0.3 to 0.5 pA . The data were collected when the chamber pressure reached 10^{-9} Torr.

Two-dimensional ion mapping of the electrode was obtained by using TOF-SIMS (TRIFT V, ULVAC-PHI Inc.). The electrodes were bombarded by Bi_3^{2+} cluster ions (30 kV) with primary ion current at 0.059 pA .

RESULTS AND DISCUSSION

Electrochemical Reactivity of $\text{Li}_{1.2}\text{Co}_{0.13}\text{Ni}_{0.13}\text{Mn}_{0.54}\text{O}_2$. To evaluate the electrochemical reactivity of $0.5\text{Li}_2\text{MnO}_3$ – $0.5\text{LiCo}_{1/3}\text{Ni}_{1/3}\text{Mn}_{1/3}\text{O}_2$ (or $\text{Li}_{1.2}\text{Co}_{0.13}\text{Ni}_{0.13}\text{Mn}_{0.54}\text{O}_2$), galvanostatic oxidation (charge)/reduction (discharge) cycle tests

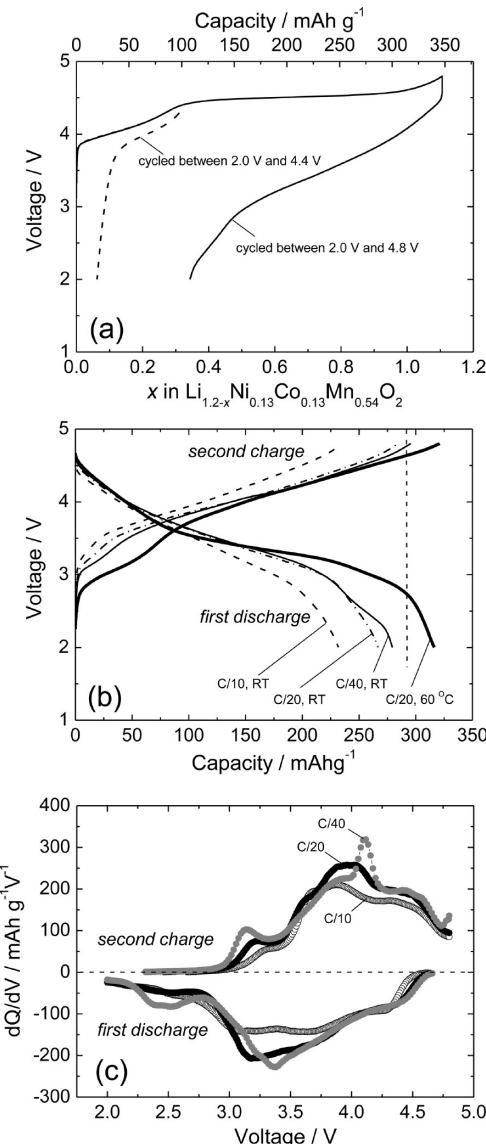


Figure 1. (a) Charge/discharge curves of the $\text{Li}/\text{Li}_{1.2}\text{Ni}_{0.13}\text{Co}_{0.13}\text{Mn}_{0.54}\text{O}_2$ cells (first cycle) in the voltage ranges of 2.0 – 4.4 and 2.0 – 4.8 V in 1 M LiPF_6 (EC/DMC) at a rate of $C/20$ (15.7 mA g^{-1}). (b) Comparison of the first discharge and second charge curves of the $\text{Li}/\text{Li}_{1.2}\text{Ni}_{0.13}\text{Co}_{0.13}\text{Mn}_{0.54}\text{O}_2$ cells at different rates in the voltage range of 2.0 – 4.8 V at 25 or 60°C . (c) Differential capacity (dQ/dV) plots of the first discharge and second charge curves of the $\text{Li}/\text{Li}_{1.2}\text{Ni}_{0.13}\text{Co}_{0.13}\text{Mn}_{0.54}\text{O}_2$ cells, which were calculated from the data shown in (b). Additional redox peaks (2.5 V in discharge and 4.1 V in charge) are confirmed at the lowest current density of $C/40$ (7.9 mA g^{-1}).

were conducted with different voltage limits vs Li/Li^+ . Figure 1a compares the voltage profiles of the $\text{Li}/\text{Li}_{1.2}\text{Co}_{0.13}\text{Ni}_{0.13}\text{Mn}_{0.54}\text{O}_2$ cells in the initial cycles. The cells were cycled with different voltage ranges (4.4 or 4.8 V cutoff) at a rate of $C/20$ (15.8 mA g^{-1}) at room temperature. In this Article, C-rate was based on one electron redox per a formula unit of $\text{Li}_{1.2}\text{Co}_{0.13}\text{Ni}_{0.13}\text{Mn}_{0.54}\text{O}_2$, whose capacity was calculated to be 314 mAh g^{-1} . When the voltage range is limited to 4.4 V , first charge capacity of 100 mAh g^{-1} is observed, corresponding to that for the removal of approximately 0.3 mol of lithium ions from $\text{Li}_{1.2}\text{Co}_{0.13}\text{Ni}_{0.13}\text{Mn}_{0.54}\text{O}_2$. On further charging up from 4.4 to 4.8 V , the characteristic voltage plateau ($\sim 250 \text{ mAh g}^{-1}$) appears. If it is

assumed that the current observed across the voltage plateau is consumed by the lithium extraction without any side reactions, an additional 0.8 mol of lithium ions is extracted in the range of 4.4–4.8 V. The charging capacity obviously exceeds the expected values based on the $\text{Ni}^{2+}/\text{Ni}^{4+}$ and $\text{Co}^{3+}/\text{Co}^{4+}$ redox reaction (approximately 120 mAh g⁻¹). The extra charging capacity (250–270 mAh g⁻¹) beyond the limit based on the tetravalent transition metals is closely related to the characteristic feature of Li_2MnO_3 , possibly simultaneous removal of lithium and oxide ions.^{18,34–36} The first discharge capacity of the $\text{Li}/\text{Li}_{1.2}\text{Co}_{0.13}\text{Ni}_{0.13}\text{Mn}_{0.54}\text{O}_2$ cell reaches 260 mAh g⁻¹ after the charging to 4.8 V at a (1/20)C rate (15.7 mA g⁻¹). The observed capacity corresponds to approximately 0.7 mol of lithium ions based on the formula unit of $\text{Li}_{1.2}\text{Co}_{0.13}\text{Ni}_{0.13}\text{Mn}_{0.54}\text{O}_2$. The voltage profile of first discharge is, however, completely deviated from the first charge curve, suggesting a permanent structural change upon the initial charge.

The rechargeable capacity of the $\text{Li}/\text{Li}_{1.2}\text{Co}_{0.13}\text{Ni}_{0.13}\text{Mn}_{0.54}\text{O}_2$ cell is strongly influenced by the operating temperature. First, discharge and second charge curves of the $\text{Li}/\text{Li}_{1.2}\text{Co}_{0.13}\text{Ni}_{0.13}\text{Mn}_{0.54}\text{O}_2$ cells operated at 25 and 60 °C are compared in Figure 1b. The observed rechargeable capacity at 60 °C exceeds 300 mAh g⁻¹ at (1/20)C rate. Note that when one electron reduction based on the transition metals (i.e., $\text{Co}^{3+}/\text{Co}^{4+}$, $\text{Ni}^{3+}/\text{Ni}^{4+}$, and $\text{Mn}^{3+}/\text{Mn}^{4+}$) is assumed for $\text{Li}_{1.2}\text{Co}_{0.13}\text{Ni}_{0.13}\text{Mn}_{0.54}\text{O}_2$, the rechargeable capacity can be calculated to be 251 mAh g⁻¹. The estimated rechargeable capacity increases to 290 mAh g⁻¹ when $\text{Ni}^{2+}/\text{Ni}^{4+}$ redox via Ni^{3+} is assumed. The observed discharge capacity (>300 mAh g⁻¹) at 60 °C for the first discharge is, however, slightly larger than the estimated value based on the solid-state redox of the transition metal ions.

The voltage profile of the first discharge curves on the $\text{Li}/\text{Li}_{1.2}\text{Co}_{0.13}\text{Ni}_{0.13}\text{Mn}_{0.54}\text{O}_2$ cells operated at different current density is also shown in Figure 1b. Three independent cells were charged at the same rate of (1/20)C at room temperature, and then discharged at different current rates of (1/10), (1/20), and (1/40)C, corresponding to 31.6, 15.7, and 7.9 mA g⁻¹, respectively. The observed first discharge capacity of 230 mAh g⁻¹ at (1/10)C increases to 280 mAh g⁻¹ at a (1/40)C rate. Note that when the current density is reduced to (1/40)C, an additional voltage plateau at around 2.5 V is observed. Differential capacity dQ/dV (Q , capacity and V , voltage of the cells) plots, which were calculated from the galvanostatic curves for the first discharge and second charge operated at (1/10), (1/20), and (1/40)C rates in Figure 1b, are shown in Figure 1c. For the first discharge at (1/20)C rate, broad and multiple peaks centered at around 4.3, 3.7, and 3.1 V are confirmed. For the second discharge at (1/20)C rate, similar broadened peaks centered at 3.2, 3.9, and 4.4 V are observed. New peaks are visible at (1/40)C rate, which are located at 2.5 V for the first discharge and 4.1 V for the second charge. According to the literature, the peak observed at 3.2 V for the charge process is related to spinel phase formation.¹⁴ These new peaks become visible only at the lower rate, and the difference in voltage of the two peaks is approximately 1.6 V. It is interesting to note that the voltage difference is very similar to that reported previously for the Li_2O_2 electrode with large polarization (~1.5 V).⁵¹ The origin of these plateaus is further discussed in a later section.

The main conclusions for the electrochemical reactivity of $\text{Li}_{1.2}\text{Co}_{0.13}\text{Ni}_{0.13}\text{Mn}_{0.54}\text{O}_2$ are the following: (i) The $\text{Li}/\text{Li}_{1.2}\text{Co}_{0.13}\text{Ni}_{0.13}\text{Mn}_{0.54}\text{O}_2$ cells show very high rechargeable capacity (>300 mAh g⁻¹ at 60 °C), which exceeds the theoretical value

based on the solid-state redox of each transition metal ($\text{Co}^{3+}/\text{Co}^{4+}$, $\text{Ni}^{2+}/\text{Ni}^{3+}/\text{Ni}^{4+}$, and $\text{Mn}^{3+}/\text{Mn}^{4+}$). (ii) When the cells were cycled at a slower current density (e.g., a (1/40)C rate), new voltage plateaus at 2.5 V for the first discharge and at 4.1 V for the second charge were observed. The difference in the voltage between the plateaus is 1.6 V, which closely resembles that of the Li_2O_2 as described below.

Structural Analysis by Synchrotron X-ray Diffraction (SXRD). SXRD was utilized for the analysis of the change in crystal structures of $\text{Li}_{1.2}\text{Co}_{0.13}\text{Ni}_{0.13}\text{Mn}_{0.54}\text{O}_2$. Powder diffraction data collected are displayed in Figure 2. The SXRD pattern of the pristine $\text{Li}_{1.2}\text{Co}_{0.13}\text{Ni}_{0.13}\text{Mn}_{0.54}\text{O}_2$ powder is shown in Figure 2a. Observed Bragg diffraction lines were indexed to a conventional hexagonal unit cell with space group symmetry of R3 except for superlattice lines observed in the 2θ range of 7–10°. The superlattice diffraction lines have a broadened peak profile, especially for the (1/3, 1/3, l)_{hex} lines, indicating that a stacking fault of the $[\sqrt{3}a_{\text{hex}} \times \sqrt{3}a_{\text{hex}}]\text{R}30^\circ$ -type superlattice layers exists along the c -axis direction. A similar trend has been found in the previous reports on the Li_2MnO_3 system.^{52,53} Lattice parameters were calculated to be $a_{\text{hex}} = 2.84953(6)$ Å, $c_{\text{hex}} = 14.2233(2)$ Å based on the R3 symmetry. Because occupancy and isotropic displacement parameters at each site are highly correlated parameters for the Rietveld analysis, the isotropic displacement parameters were restricted to the constant values based on previous studies.^{54,55} The metal fractions at the 3a and 3b sites and occupancy of the oxygen at the 6c site were refined under this restriction. The structural parameters refined by the Rietveld analysis are listed in Table 1. The ionic radii of Ni^{2+} (0.69 Å) and Li^+ (0.76 Å) are very similar for octahedral environments, but intermixing between Ni and Li ions is negligible (less than 1%). Excess Li ions (~3%) are found in the structure, indicating that the sample stoichiometry is slightly deviated from the ideal composition of $\text{Li}_{1.2}\text{Co}_{0.13}\text{Ni}_{0.13}\text{Mn}_{0.54}\text{O}_2$. This is consistent with the fact that 5% excess LiOH in molar ratio was utilized for the materials synthesis. 2% of Li might be vaporized during the calcination process, but 3% of Li ions was further accommodated in the crystal lattice, forming a slightly lithium-rich (or transition metal-deficient) phase. The excess amount of lithium ions relative to the stoichiometric condition was directly confirmed by ICP chemical analysis on the sample. The oxygen occupancy is also refined by the Rietveld analysis. Oxygen occupancy was nicely refined to 2.00(1) without any restrictions except the fixed isotropic displacement parameter, even though oxygen has a relatively small scattering factor for X-ray. Small standard deviation for the oxygen occupancy indicates that no oxygen vacancy exists in this sample. Note that all of the variables (lattice parameters, occupancy, site fractions, oxygen positional parameters, and profile parameters) in the Rietveld analysis were refined simultaneously by the nonlinear least-squares method. Nevertheless, the reproducibility of the data convergence was excellent with reasonably small standard deviations.

SXRD patterns of the $\text{Li}_x\text{Co}_{0.13}\text{Ni}_{0.13}\text{Mn}_{0.54}\text{O}_2$ electrode discharged to 2.0 V after the charging to 4.4 V is shown in Figure 2b, and the structural parameters refined by Rietveld analysis are also listed in Table 1. For the electrochemically cycled samples, the occupancy of Li was not directly refined by the Rietveld analysis to reduce the variable parameters, and the occupancy of Li was estimated as follows. The Li content for the analysis was determined by the current passed through the composite electrode with the assumption that all charges were

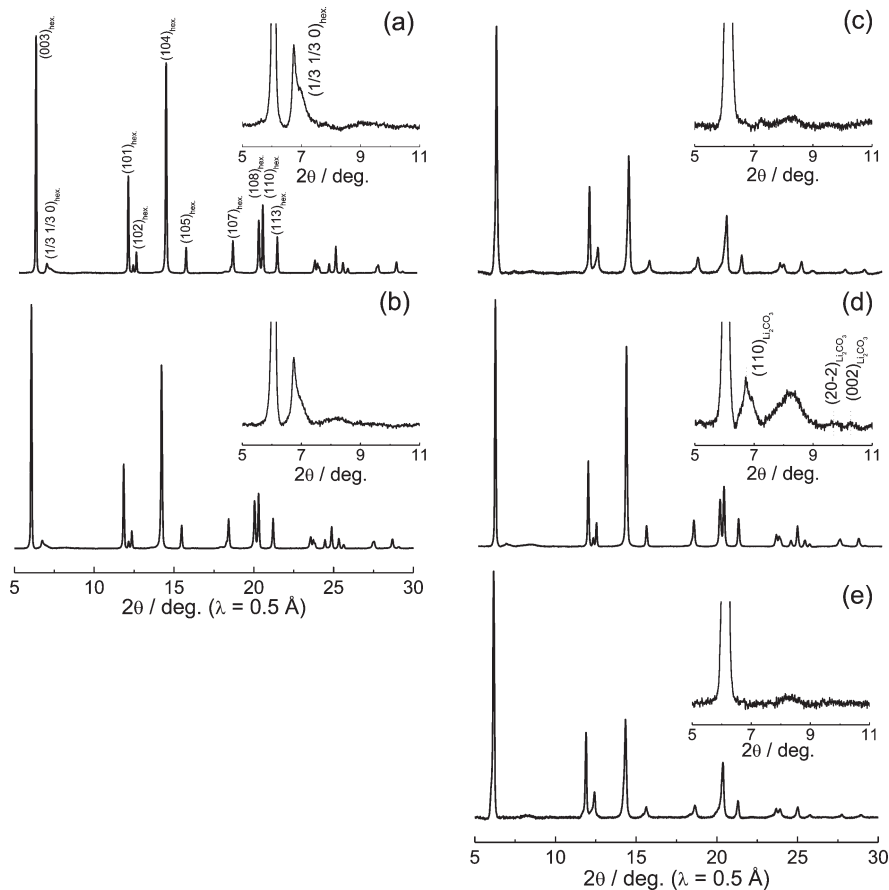


Figure 2. Synchrotron powder X-ray diffraction patterns of $\text{Li}_x\text{Ni}_{0.13}\text{Co}_{0.13}\text{Mn}_{0.54}\text{O}_2$ samples: (a) pristine material, charged to (b) 4.4 V or (c) 4.8 V, (d) discharged to 2.0 V after the charging to 4.8 V, and (e) recharged to 4.8 V after the initial charge/discharge cycle in the voltage range of 2.0–4.8 V in 1 M LiPF_6 (EC/DMC) at room temperature. Detailed crystallographic parameters are summarized in Table 1. Highlighted X-ray diffraction patterns related to the in-plane superlattice ordering of lithium and transition metals are shown in the insets in the 2θ range of 5–11°.

consumed by the lithium extraction process without any side reactions such as electrolyte decomposition. Total site occupancy of the lithium ion at 3a and 3b sites is slightly reduced (approximately 7%) as compared to that of as-prepared sample because of the irreversible capacity during the first charge/discharge cycle. In addition to this assumption, the site fractions of Li at 3a and 3b sites were decided on the basis of the previous NMR study reported on the lithium nickel manganese layered oxides.^{20,56} The NMR study revealed that lithium ions locating at the 3b site (metal site) are electrochemically active as well as the lithium ions in the 3a site (lithium layer), and it seems to be a partly reversible process. Therefore, the vacancy at the lithium sites was equally created at 3a and 3b sites for the discharged sample. Other refined crystallographic parameters including the oxygen occupancy, the full-width at half-maximum (fwhm) of the Bragg diffraction lines, and peak intensity of the superlattice diffraction lines are almost identical as shown in Figure 2 and Table 1, indicating that a reversible solid-state redox reaction occurs without the structural modifications associated with transition metal/oxygen migration below 4.4 V before the voltage plateau.

SXRD analysis revealed that the structural modification evidently proceeds when the electrode was charged to 4.8 V beyond the voltage plateau. Figure 2c shows the SXRD pattern collected from the charged state. The peak profile of all diffraction lines broadened and changed to an asymmetrical shape, which are

clearly different from that of the 4.4 V charged state (Figure 2b). A similar observation by neutron study was reported and explained as a small amount of residual phase in the data.³⁶ The SXRD pattern of the $\text{Li}_x\text{Co}_{0.13}\text{Ni}_{0.13}\text{Mn}_{0.54}\text{O}_{2-\delta}$ electrode discharged to 2.0 V after the charging to 4.8 V is represented in Figure 2d. The peak profile recovers from the broad and asymmetrical shape observed at the 4.8 V charged state to the sharp and symmetrical profile after the discharge to 2.0 V. In this study, the Rietveld analysis was conducted in the sample of discharged state because the well-defined Bragg diffraction lines with the symmetrical peak profile allow us to analyze the data using a simple single phase model. The findings in comparison to the pristine sample are summarized as follows: (1) lattice parameters increase from $a_{\text{hex}} = 2.85$ to 2.86 \AA and $c_{\text{hex}} = 14.22$ to 14.28 \AA , (2) fwhm of the peak profile becomes wider, for example, from 0.076° to 0.106° in 2θ angle for the $(110)_{\text{hex}}$ diffraction line, (3) the superlattice diffraction lines disappear, (4) occupancy of the oxygen decreases from $2.00(1)$ to $1.85(1)$ when it is allowed to be refined, and (5) occupancy of transition metals increases at the lithium layer ($\sim 5\%$). The results suggest that the oxygen removal from the bulk of the particles leads to structural reconstruction including the in-plane cation rearrangement process and the migration process from the metal to lithium layer. This is no longer the reversible solid-state redox reaction accompanied by lithium insertion/extraction into/from the crystal lattice. As the model of the structural modification, the oxygen vacancy model

Table 1. Crystallographic Parameters Refined by the Rietveld Method on the Synchrotron X-ray Diffraction Patterns of $\text{Li}_{1.2}\text{Ni}_{0.13}\text{Co}_{0.13}\text{Mn}_{0.54}\text{O}_2$ and the Electrochemically Cycled Samples (Discharged to 2.0 V after the Charging to 4.4 or 4.8 V)^a

	pristine	4.4 V discharged state	4.8 V discharged state
composition	$\text{Li}_{1.226}\text{MeO}_{2-\delta}^c$	$\text{Li}_{1.16}\text{Me}_{0.774}\text{O}_{2-\delta}^{b, c}$	$\text{Li}_{0.92}\text{Me}_{0.774}\text{O}_{2-\delta}^{b, c}$
space group	R3	R3	R3
lattice constants (\AA)	a_{hex} c_{hex}	2.84952(6) 14.2233(2)	2.85135(6) 14.2307(3)
unit cell volume (\AA^3)	V_{hex}	100.017(4)	100.197(4) 101.365(4)
3a site	Me (g) ^c Li (g) B (\AA^2)	0.768(1) ^e 0.233(1) 0.20 ^d	0.768(1) ^e 0.22 ^d 0.20 ^d
3b site	Li (g) Me (g) ^c B (\AA^2)	0.994(1) 0.006(1) ^e 0.9 ^d	0.95 ^d 0.006(1) ^e 0.9 ^d
6c site	O (g) B (\AA^2)	1.000(5) 0.60 ^d	1.001(5) 0.60 ^d
z for 6c site	O	0.2586(2)	0.2588(2) 0.2586(2)
fwhm (deg)	(003) _{hex} (104) _{hex} (110) _{hex}	0.068 0.082 0.076	0.0772 0.086 0.086
R_{wp} (%)	4.19	3.04	2.84
R_{I} (%)	3.62	4.26	3.41

^a Oxygen amount is clearly reduced by the charging across the voltage plateau, and occupation of the transition metals at the lithium sites clearly increases. ^b Estimated from current passed through the composite electrode with assumed 100% columbic efficiency. ^c Imaginary chemical species (16% Ni, 16% Co, and 68% Mn) were used. ^d Not refined. ^e Total metal occupancy per the formula unit was refined to 0.774 for the pristine sample. The total metal amount was fixed based on this value for the analysis of the electrochemically cycled samples.

(or oxygen diffusion model)¹⁸ was utilized for the Rietveld analysis in this study. Simulated XRD patterns with or without refining the oxygen occupation in that this model leads to the creation of the oxygen vacancies in the lattice are shown in Supporting Information Figure S1. Although the atomic scattering factor of oxygen is relatively small for the X-ray diffraction, the assumption of the oxygen vacancy formation in the crystal lattice drastically reduces reliable factors as shown in Supporting Information Figure S1. A clear difference is observed for the (102)_{hex} diffraction line. Moreover, its standard deviation is significantly smaller than the amount of oxygen vacancy created in the crystal lattice. Another model proposed is the transition metal densification model (or transition metal migration model).^{35,36} However, it is quite difficult to distinguish which model is more appropriate to describe the crystal structure of the sample (see Supporting Information Figure S2 in detail) as also pointed out by Croguennec and co-workers.³⁵ Note that both models almost equally argue oxygen removal and change in the ratio of metal to oxygen from the crystal lattice. The only difference is the diffusion species (oxygen vs transition metals) after the oxygen removal at the surface. In the oxygen vacancy diffusion model, ideally the cation distribution in the lattice was not changed. However, the disappearance of the superlattice diffraction lines suggests that, at least to some extent, the in-plane transition metal arrangement changes. In addition to the in-plane cation rearrangement, the change in the cation distribution in the crystal lattice was directly confirmed by Rietveld analysis. Refined cation distribution of the sample after charging to 4.8 V is described as $[\text{Li}_{0.75}\text{Me}_{0.05}\square_{0.20}]_{3b}[\text{Li}_{0.17}\text{Me}_{0.73}\square_{0.10}]_{3a}\text{O}_{1.85}$ by applying the oxygen vacancy model (or $[\text{Li}_{0.81}\text{Me}_{0.05}\square_{0.14}]_{3b}[\text{Li}_{0.18}\text{Me}_{0.78}\square_{0.04}]_{3a}\text{O}_2$ by using the densification model). In the pristine sample, occupation of transition metals in the lithium

layer (3b site) was negligible. In contrast, ~5% of transition metals are found after the cycling to the voltage plateau. This is consistent with the result found in a study by Gray and co-workers,²² and behavior different from that of $\text{LiNi}_{0.5}\text{Mn}_{0.5}\text{O}_2$, in which nickel ions migrated from the lithium to the metal layer during charging.^{54,56} Oxygen removal from the lattice is estimated to be 0.15 mol per the formula unit (ca. 7.5% of oxygen in the lattice) by Rietveld analysis. When it is assumed that current passed through the composite electrode beyond the oxidation limit of Co^{4+} , Ni^{4+} , and Mn^{4+} is ideally compensated by the simultaneous Li^+ and O^{2-} removal process from the crystal lattice, the amount of oxygen reaches 0.355 mol ($\text{Li}_{0.92}\text{Me}_{0.77}\text{O}_{1.65}$ as the chemical formula, corresponding to 18% of oxygen removal), which is a much larger amount of oxygen in comparison to that estimated by the Rietveld analysis. Because some of experimental restrictions were used (e.g., fixed isotropic displacement parameters) in the Rietveld analysis, there is little ambiguity about the quantitative amount of oxygen removed from the lattice. A similar finding was noted in the study of the pure Li_2MnO_3 by quantitative analysis of oxygen gas generated from the crystal lattice.³⁴ The detected amount of oxygen gas was approximately 50% of the estimated value if no Li^+/H^+ exchange was assumed. These results suggest that lithium ions are partly removed without oxygen release, which is further discussed in a later section.

In summary, the changes in the bulk crystal structures of $\text{Li}_{1.2}\text{Co}_{0.13}\text{Ni}_{0.13}\text{Mn}_{0.54}\text{O}_2$ are described as follows: (i) oxygen atoms are removed from the crystal lattice by the initial charge to voltage plateau, causing the cation rearrangement process including the migration of transition metals to the lithium layer (~5%), and (ii) the amount of oxide ions removed from the crystal lattice reaches approximately 7.5%, which is less than one-half of the

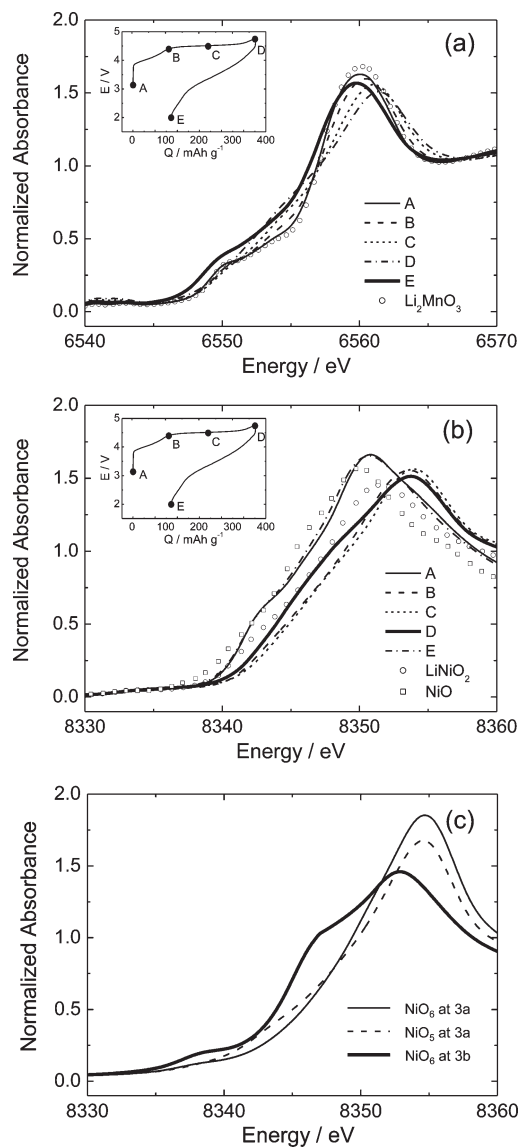


Figure 3. XANES spectra of $\text{Li}_x\text{Ni}_{0.13}\text{Co}_{0.13}\text{Mn}_{0.54}\text{O}_{2-\delta}$ collected at (a) Mn K-edge and (b) Ni K-edge during the initial charge/discharge cycle in the voltage range of 2.0 and 4.8 V in 1 M LiPF_6 (EC/DMC) as electrolyte. The points, where XAS measurements were carried out, are shown in the insets. XANES spectra of Li_2MnO_3 , NiO , and LiNiO_2 as reference samples are also shown. (c) Ni K-edge XANES spectra were simulated to interpret the observed data in the charged state. XANES spectra were calculated from three different nickel environments, which show clearly different spectra (see the text in detail).

expected value (18%) based on the limit of the tetravalent transition metals and continuous oxygen loss at the voltage plateau.

Electronic and Local Structures by X-ray Absorption Spectroscopy (XAS). XAS was utilized to further study the reaction mechanisms related to the charge compensation process. X-ray absorption near-edge structures (XANES) spectra, collected at Mn K-edge (6539 eV) and Ni K-edge (8333 eV), are plotted in Figure 3. Figure 3a shows manganese K-edge XANES spectra observed during the charging up to 4.8 V, and points where the spectra were collected in the charge and discharge curves are shown in the inset of the figures. The XANES spectrum of the pristine sample at the Mn K-edge resembles that of

Li_2MnO_3 . The shape of the spectra continuously changes during the charging, but the inflection point of the K-edge spectra stays at a constant value at approximately 6556 eV. It is speculated that shape of the spectra is influenced by the modification of the local structures, for example, the removal of lithium ions, forming the vacancy at the octahedral 3a/3b sites neighboring manganese ions. The electronic structures are easily influenced by the local structures without the change in formal oxidation states of the manganese ions.

In a sample that was discharged to 2.0 V after charging to 4.8 V, a clear difference is confirmed in the XANES spectra at the Mn K-edge. The spectrum of the discharged sample is located entirely to the lower energy region than that of the pristine sample, indicating that manganese ions are partly reduced from the tetravalent to trivalent state. Note that this observation was not seen for the 4.4 V cycle. The spectrum recovers to the same profile and energy as the pristine sample when the cell is cycled in the voltage range of 2.0 and 4.4 V. The energy of the Mn K-edge spectra again shifts to the higher energy for the second charge to 4.8 V (not shown), suggesting that the manganese ions become redox reactive species for the subsequent cycles after charging to the high voltage plateau. Recently, a similar observation has been reported in the “pure” Li_2MnO_3 for the discharged sample after the charging to the high voltage.³⁴ In contrast to these observations, reduction of the manganese ions to the trivalent state was not observed in $\text{Li}[\text{Li}_{1/9}\text{Ni}_{1/3}\text{Mn}_{5/9}] \text{O}_2$.²² The difference might originate from the amount of Li_2MnO_3 component, correlating closely with the amount of oxygen removed from the lattice and the structural rearrangement processes. Further systematic study is needed to generalize this finding to the lithium-excess manganese layered oxides.

The change in the electronic structures of the Ni ions was also examined by XAS. XANES spectra collected at Ni K-edge during the charging up to 4.8 V are shown in Figure 3b. The spectrum profile of the pristine sample is slightly different from rocksalt-type Ni^{2+}O , which is located in the higher energy region. This is consistent with the fact that a Li-excess (~3%) composition is found by the Rietveld analysis in Figure 2 and Table 1, that is, charge compensation by the nickel oxidation, resulting in the partial oxidation of divalent nickel ions to the trivalent state. A similar charge compensation process by the nickel ion oxidation is typically found for the Li-excess $\text{LiNi}_{0.5}\text{Mn}_{0.5}\text{O}_2$ system.^{57,58} The energy of nickel K-edge shifts to the higher energy region as the Li content increases because of the nickel oxidation. When $\text{Li}_{1.2}\text{Co}_{0.13}\text{Ni}_{0.13}\text{Mn}_{0.54}\text{O}_2$ is charged to 4.4 V, the energy of the XANES spectrum shifts to the higher energy region (~2.5 eV), indicating that nickel ions are oxidized from divalent/trivalent mixed state to the trivalent/tetravalent mixed state. On further charging up to the middle of the voltage plateau (point C in the inset of Figure 3b; $x = 0.48$ in $\text{Li}_x\text{Co}_{0.13}\text{Ni}_{0.13}\text{Mn}_{0.54}\text{O}_{2-\delta}$), the peak profile slightly changed in comparison to the 4.4 V charged state, but no significant change in the K-edge energy is observed. The spectrum profile evidently changes after charging to 4.8 V. The energy slightly shifts to the lower energy region during the “charging (oxidation)” process.

To interpret the XANES spectrum of the 4.8 V, a simulation of the Ni K-edge spectra was conducted by using the FEFF program. Figure 3c shows simulated K-edge spectra of the nickel ions locating in different local environments. In the simulation, three different local environments were assumed (those schematic illustrations are shown in Supporting Information Figure S3). (a) A nickel ion is located at the octahedral 3a site, which is

the same local environment as an ideal layered structure, but one vacancy was created at the neighboring edge-shared octahedral site in the metal layer. Li ion removal from the metal layer and vacancy formation at the octahedral site were assumed in this model. (b) The environment of the nickel ion is the same as in (a), but an oxygen vacancy was created around the nickel ions. One oxygen vacancy per a NiO_6 octahedron was created, corresponding to 16.7% oxygen vacancy per a nickel ion. (c) A nickel ion is located at the octahedral 3b site (lithium layer). Considering the result obtained by Rietveld analysis (Table 1), nickel ion migration from the metal to lithium layer was assumed in this model. As shown in Figure 3c, the oxygen vacancy formation affects the electronic structure of the nickel ions located at the octahedral environment. However, the estimated difference from the simulated spectra might not be clear if the amount of the oxygen vacancies created in the crystal lattice is limited to below 8% per the formula unit as suggested by the Rietveld analysis. In contrast to the oxygen vacancy model, a marked difference is expected from the nickel ion migration process. The electronic structure of the nickel ion is drastically influenced by the migration process from the 3a to the 3b sites. It is noted that this change in the XANES spectra is achieved without a reduction process of the nickel ions and the oxygen loss from the bulk of the particles. The interatomic distance between metal and oxygen at the 3b sites (2.15 Å) is much longer than that at the 3a sites (1.89 Å) for the charged state. We believe that the shift of the absorption spectra toward the lower energy region originates from the difference in the interatomic distances. This is probably consistent with the observation that 5% transition metal ions migrated to the 3b sites after the charging to the voltage plateau.

For cobalt and manganese K-edge spectra, much more complex changes during the charging were observed. This makes the situation more complicated. It is not clear whether cobalt and manganese ions also migrate as well as nickel ions, or whether nickel ions selectively migrate during the first charging process. If it is hypothesized that 5% cation migration suggested by Rietveld analysis was achieved by a selective nickel migration process, this corresponds to ca. 35% of the nickel ions in $\text{Li}_x\text{Co}_{0.13}\text{Ni}_{0.13}\text{Mn}_{0.54}\text{O}_{2-\delta}$ migrating from the metal to the lithium layer.

Recently, a similar shift in the Ni K-edge XAS spectra to the lower energy level during charging has been reported for the Li-excess system, and it has been proposed that the nickel ions are reduced at the oxide surface by the electrolyte.²² This process might result in the film formation at the surface of the oxide particles as decomposed products of the electrolyte. The surface analysis on the electrode by X-ray photoelectron spectroscopy will be discussed in a later section.

In conclusion, the electronic structure and local structures of the $\text{Li}_x\text{Co}_{0.13}\text{Ni}_{0.13}\text{Mn}_{0.54}\text{O}_{2-\delta}$ were examined by XAS in this section. After the charging to the voltage plateau, tetravalent manganese ions were partly reduced to the trivalent state on discharge. Manganese ions became electrochemically active in the subsequent cycles. By comparing the results between observed and simulated nickel K-edge spectra, it was estimated that the nickel ion partly migrated from the metal to lithium layer during the charging to the voltage plateau. The present XAS study further supported the structural rearrangement confirmed by Rietveld analysis.

The Charge Compensation Mechanism of $\text{Li}_x\text{Co}_{0.13}\text{Ni}_{0.13}\text{Mn}_{0.54}\text{O}_{2-\delta}$. In the case of the solid-state redox reaction of the electrode materials, the electrons are removed from/injected at the

Fermi level. If the electrochemical potential of the materials is slightly lower than 4 V (vs Li/Li⁺), the Fermi level of materials mainly consists of transition metal 3d-orbitals (e.g., Fe²⁺/Fe³⁺ in LiFePO_4 ⁵⁹), because the energy level of filled oxygen 2p-orbitals is located in a much lower level than that of partially filled metal 3d-orbitals. This is simply described as an ionic bond between the metal and oxide ions, and it is easy to image that electrons are removed from the 3d orbitals of the transition metals by the oxidation to compensate the charge accompanied with the lithium extraction process. In contrast to the ionic materials, when the electrochemical potential of the system increases to ~5.0 V vs Li, the energy level of 3d-orbitals for the metals (e.g., Mn⁴⁺, Co⁴⁺, Ni⁴⁺, etc.) approaches that of the oxygen 2p-orbital, increasing the covalency of the Me–O bond. The Fermi level of materials having the covalent character is therefore generally composed of both oxygen 2p-orbitals and transition metal 3d-orbitals. A first-principles calculation on Li_2MnO_3 has suggested that lithium ions are removed from the lattice without the oxygen loss at 4.6 V vs Li/Li⁺, and electrons were removed from both oxygen 2p-orbitals and manganese 3d-orbitals, which compensate for the charge removed from the lattice.⁶⁰ Although it is not easy to define the redox species in the case of highly covalent materials (like Li_2MnO_3), the first-principles study proposed that oxygen works as the redox species during the charging process without the release of oxygen gas. Soft XAS study at oxygen K-edge on $\text{Li}_{1-x}\text{Co}_{1/3}\text{Ni}_{1/3}\text{Mn}_{1/3}\text{O}_2$ directly detected the increased vacancy (or hole) of the oxygen 2p during charging.⁶¹ These experimental data also suggest that oxygen plays an important role as the redox species in the covalent materials, even if the case when a highly reversible electrode system, which does not release oxygen gas (like $\text{Li}_{1-x}\text{Co}_{1/3}\text{Ni}_{1/3}\text{Mn}_{1/3}\text{O}_2$), is charged to the high voltage. A major inconsistency between the first-principles calculation and the experimental observations on the Li_2MnO_3 system is the oxygen loss associated with the cation migration process as discussed in the previous sections. It should be noted that the first-principles calculation based on a density functional theory deals with the electronic structure of bulk crystal using a band model. For the composite electrodes in the electrochemical cells, materials surface contacts with aprotic electrolyte solution, acetylene black, and PVdF. The oxygen generation reaction at the electrolyte/particle interface would be catalyzed by the existence of these materials. In addition, the electrolyte solution might chemically reduce the particle surface, leading to the carbon dioxide/monoxide generation.^{22,34} Thus, it is speculated that these reactions generate oxygen vacancy at the electrode surface and propagate the structural modification to the inside particles as observed by SXRD and XAS. However, the amount of the oxygen vacancies generated in the lattice is always smaller than the expected value based on the simultaneous Li⁺ and O²⁻ removal process (Li₂O removal) during the voltage plateau. It was confirmed by SXRD in $\text{Li}_x\text{Co}_{0.13}\text{Ni}_{0.13}\text{Mn}_{0.54}\text{O}_{2-\delta}$ and by quantitative gas analysis in Li_2MnO_3 .³⁴ From these observations and considerations, it is assumed that electron removal from the oxygen 2p-orbital and metals t_{2g}-orbitals, which are the main components near the Fermi level, partly compensates for the excess charge without oxygen loss as suggested by the first-principles calculation.⁶⁰ Meanwhile, the Fermi level of the material is reconstructed by the partial oxygen loss from the particles. The vacancy or hole created at the Fermi level during the high voltage plateau is partly lost by the oxygen removal processes, lowering the average oxidation state of the materials without the electrochemical reduction (lithium insertion) process. Consequently, the energy level of manganese empty e_g-orbital is closer to the Fermi level than in the sample before charging. The XAS results for $\text{Li}_x\text{Co}_{0.13}\text{Ni}_{0.13}\text{Mn}_{0.54}\text{O}_{2-\delta}$

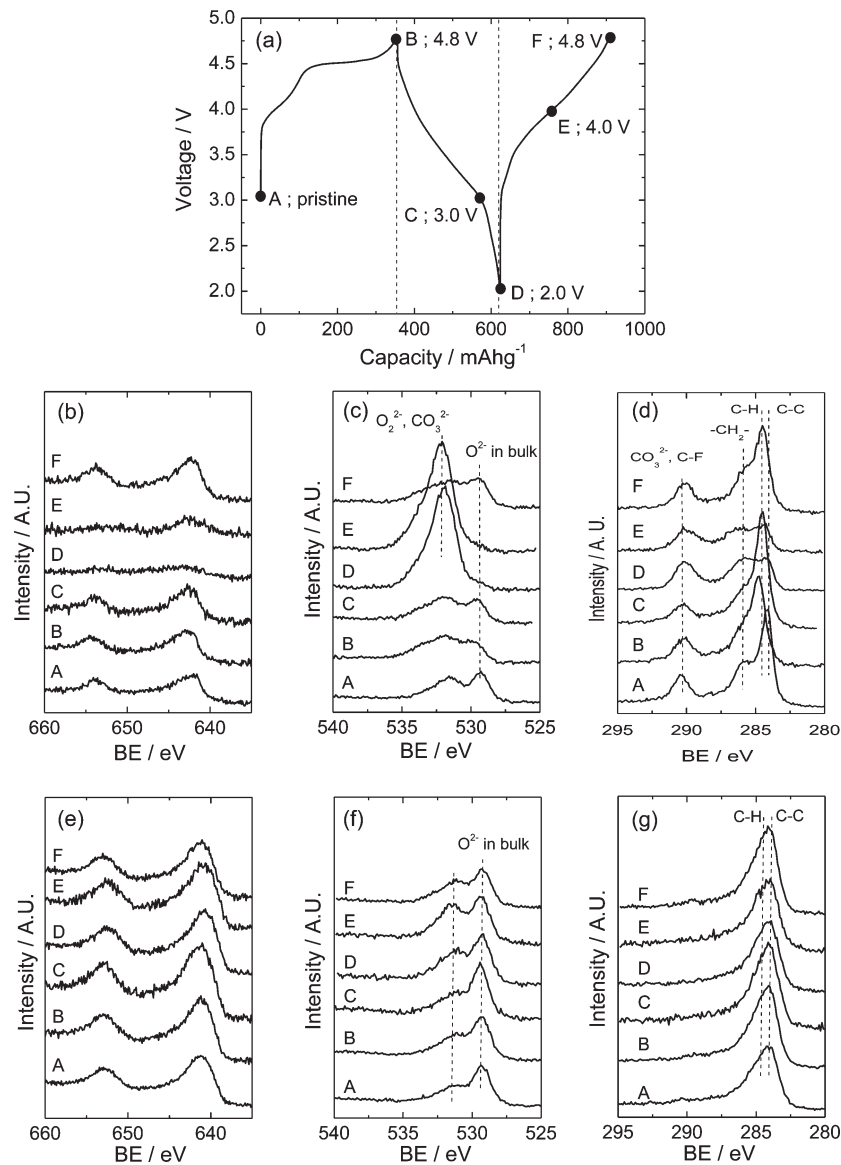


Figure 4. XPS spectra of the $\text{Li}_x\text{Ni}_{0.13}\text{Co}_{0.13}\text{Mn}_{0.54}\text{O}_{2-\delta}$ composite electrodes. The locations A–F, where the measurements were conducted to the second charge process, are shown in (a). XPS spectra were collected in (b) Mn 2p, (c) O 1s, and (d) C 1s regions, and the XPS spectra of the electrodes, which were collected after the Ar^+ etching, are also shown in parts e–g, respectively. Oxygen-rich deposits are found on the electrode surface below 2.0 V. The deposits disappear by the charging process beyond 4.0 V.

revealed that the manganese ions were partly reduced to the trivalent state after the discharge to 2.0 V. If the lithium extraction/insertion occur reversibly without the oxygen loss as suggested by the first-principle study,⁶⁰ an empty e_g -orbital cannot be accessed by discharge. This fact also supports the partial oxygen loss from the materials after the charging to the voltage plateau.

In this section, the results obtained from SXRD and XAS were combined and discussed in terms of the charge compensation mechanism of the Li-excess manganese layered oxides. From the next section, the results of surface analysis in $\text{Li}_x\text{Co}_{0.13}\text{Ni}_{0.13}\text{Mn}_{0.54}\text{O}_{2-\delta}$ are discussed in detail.

Analysis on the Electrode Surface by X-ray Photoelectron Spectroscopy (XPS). XPS has been utilized to examine the change in the surface of the electrochemically cycled electrodes. Figure 4 shows the X-ray photoelectron spectra observed for manganese 2p, oxygen 1s, and carbon 1s regions during the

electrochemical cycling in the voltage range of 2.0–4.8 V. The points where the spectra were collected are plotted in Figure 4a.

(1) Mn 2p XPS spectra: Figure 4b shows the Mn 2p spectra, which mainly reflect the existence of the $\text{Li}_x\text{Co}_{0.13}\text{Ni}_{0.13}\text{Mn}_{0.54}\text{O}_{2-\delta}$ oxide particles in the surface of the composite electrodes. Two peaks are observed, which can be assigned to the manganese $2p_{3/2}$ at 642 eV and $2p_{1/2}$ at 654 eV. These energies are in good agreement with the literature data on MnO_2 .⁶²

When the $\text{Li}_{1.2}\text{Co}_{0.13}\text{Ni}_{0.13}\text{Mn}_{0.54}\text{O}_2$ composite electrode was charged to 4.8 V, the oxygen loss and cation rearrangement process was confirmed by Rietveld analysis as discussed in the previous sections. No significant change is, however, observed by XPS in this experimental condition (Figure 4b,B). It is surprising that, although the applied voltage during the charging is very high (~4.8 V), the oxide particles were not covered with a thick organic

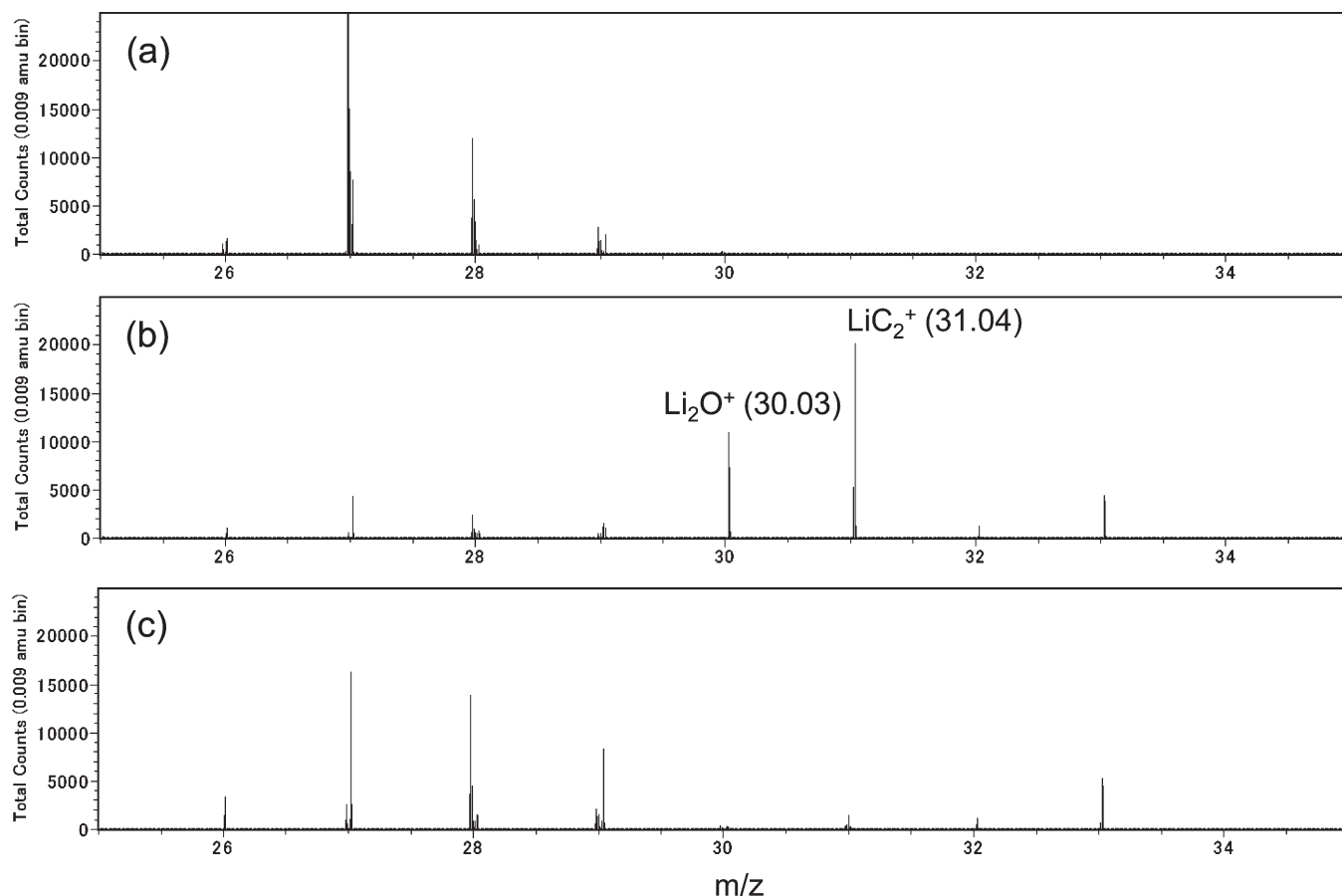


Figure 5. Comparison of TOF-SIMS spectra in the cycled $\text{Li}_x\text{Ni}_{0.13}\text{Co}_{0.13}\text{Mn}_{0.54}\text{O}_{2-\delta}$ electrodes: (a) charged to 4.8 V, (b) discharged to 2.0 V after the charging to 4.8 V, and (c) recharged to 4.8 V in 1 M LiPF_6 (EC/DMC). The fragments of Li_2O^+ and LiC_2^+ are detected in the discharged electrode.

component, such as decomposition products of electrolyte. This result probably suggests that nonaqueous electrolyte is stable and Li^+/H^+ ion-exchange is negligible during charge to the high voltage plateau. Upon the discharging from 4.8 to 3.0 V, no change in the spectra is observed. It is noted that the intensity of Mn 2p XPS spectrum is significantly reduced during the discharge from 3.0 to 2.0 V (Figure 4b,D). The intensity of the spectra recovers after the Ar^+ etching for 20 s (Figure 4e,D). In general, because electrolyte solution is electrochemically stable in this potential range, this observation suggests that the composite electrode was covered with surface deposits, which might be formed by the electrochemical reaction. The intensity of the Mn 2p XPS spectrum remains weak after the second charging to 4.0 V (Figure 4b,E). The surface deposit is electrochemically stable below 4.0 V once it is formed on the oxide surface. After the second charging to 4.8 V, the peak intensity of Mn 2p XPS spectra almost recovers to that of the pristine electrode, indicating that the surface deposits on the oxides disappear, possibly by the electrochemical decomposition above 4.0 V.

- (2) O 1s XPS spectra: In contrast to the finding for the Mn 2p XPS spectra, the oxygen 1s XPS spectra show a trend opposite to that shown in Figure 4c. The O 1s XPS spectrum, in the as-prepared electrode, is mainly composed of two components. One is an oxide ion (O^{2-}) in the crystal lattice at 529 eV, and another is the carbonate species

CO_3^{2-} at ca. 532 eV. The observation of the carbonate species would suggest the existence of Li_2CO_3 near the surface of the oxide particles because the over stoichiometric condition (5% excess Li) was used for the synthesis of $\text{Li}_{1.2}\text{Co}_{0.13}\text{Ni}_{0.13}\text{Mn}_{0.54}\text{O}_2$. When the electrode is charged to 4.8 V, the intensity of the peak assigned to oxide ion in the lattice is reduced in comparison to the carbonate species (Figure 4c,B). There are, however, subtle differences between the spectra, which are consistent with the results in the Mn 2p spectra.

- During the first discharge process, no change is observed above 3.0 V, but the peak centered at 532 eV has considerably grown after the discharging to 2.0 V. Moreover, the peak disappears on Ar^+ etching (Figure 4f,D), clearly indicating the formation of the surface deposits, which contains oxygen atoms. The grown peak is still visible after the second charge to 4.0 V (Figure 4c,E), and then disappears during the further charging from 4.0 to 4.8 V (Figure 4c,F). After the second charge to 4.8 V, the O 1s spectrum becomes comparable in intensity to that of the first charged state to 4.8 V, suggesting that the surface deposits containing oxygen were electrochemically decomposed above 4.0 V in the second charge process.
- (3) Carbon 1s XPS spectra: Figure 4d represents the carbon 1s XPS spectra observed for the $\text{Li}_{1.2}\text{Co}_{0.13}\text{Ni}_{0.13}\text{Mn}_{0.54}\text{O}_2$ composite electrodes, which contain acetylene black as a conductive agent and PVdF as a polymer binder. The C 1s spectra can be deconvoluted to several

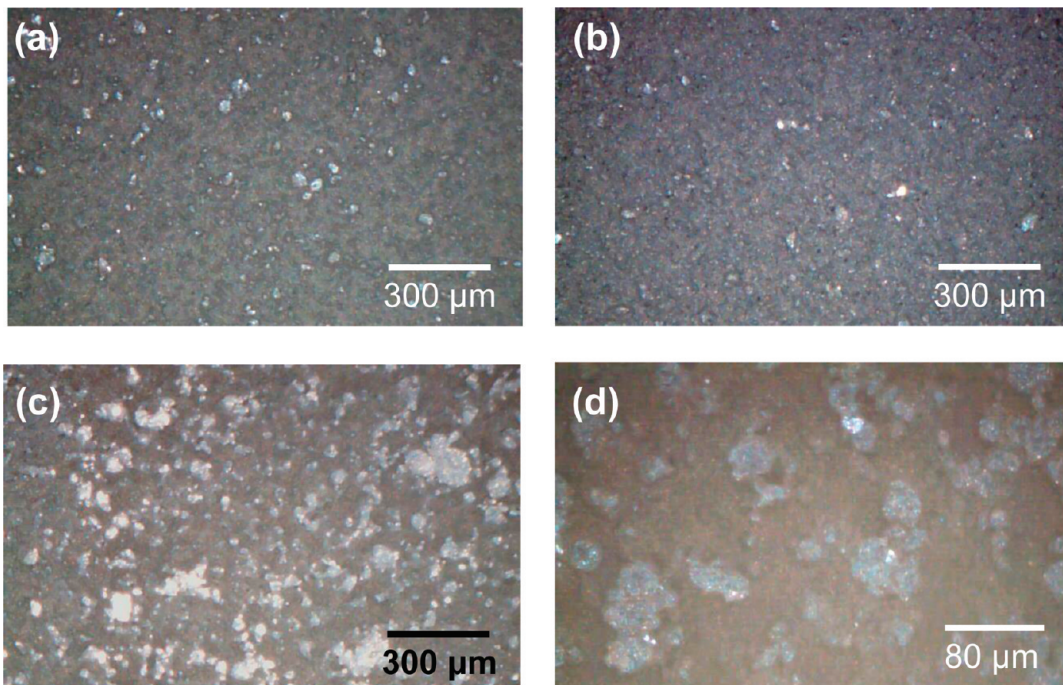


Figure 6. Top surfaces of the $\text{Li}_x\text{Ni}_{0.13}\text{Co}_{0.13}\text{Mn}_{0.54}\text{O}_{2-\delta}$ electrodes observed by using an optical microscope: (a) As-prepared electrode, discharged to (b) 3.0 V and (c,d) 2.0 V after the charging to 4.8 V in 1 M LiPF_6 (EC/DMC) in 1 M LiPF_6 (EC/DMC).

components. Acetylene black mainly contributes to a sharp peak located at 284.5 eV, which can be assigned into the C–H and C–C components. The peaks observed at 286 and 290.5 eV can be assigned into $-\text{CH}_2-$ and $-\text{CF}-$ in the PVDF backbone, respectively.^{37,40} Upon the initial charging process to 4.8 V, intensity of the C–C component at 284.5 eV is slightly reduced, but other components are only little influenced (Figure 4d, B). No change is found after the discharge process to 3.0 V (Figure 4d,C). The intensity of the C–C and hydrocarbon C–H, which originates from the acetylene black, is evidently reduced during the discharge from 3.0 to 2.0 V (Figure 4d,D), which is the same trend as was found in the Mn 2p XPS spectra. The PVDF binder seems to be still exposed to the electrode surface, because the peak of $-\text{CH}_2-$ is still observed in the spectra. The profile of the spectra is not affected during the second charge process to 4.0 V and recovers to the original surface state during the second charging from 4.0 to 4.8 V. Although the organic components are severely damaged by the Ar^+ etching, the peak related to acetylene black is observed after the etching for 20 s (Figure 4g). The surface deposits formed on acetylene black below 3 V were removed by etching (Figure 4g,D,E). The results are entirely consistent with those of the Mn 2p and O 1s spectra.

- (4) Comparison of XPS spectra for a conventional system without oxygen loss: To interpret these observations, XPS spectra collected from the $\text{Li}_{1.2}\text{Co}_{0.13}\text{Ni}_{0.13}\text{Mn}_{0.54}\text{O}_2$ electrodes are compared to that of commercially supplied $\text{LiCo}_{1/3}\text{Ni}_{1/3}\text{Mn}_{1/3}\text{O}_2$. Oxygen 1s XPS spectra for the $\text{LiCo}_{1/3}\text{Ni}_{1/3}\text{Mn}_{1/3}\text{O}_2$ electrodes surface, after the charging to 4.8 V and discharging to 2.0 V, are shown in Supporting Information Figure S4. XPS spectra for the $\text{Li}_{1.2}\text{Ni}_{0.13}\text{Co}_{0.13}\text{Mn}_{0.54}\text{O}_2$ electrodes charged to 4.4 V

(before the voltage plateau) were also collected for comparison (Figure S4). For both systems, the electrochemical lithium insertion/extraction processes occur without the oxygen loss. No change in the oxygen 1s XPS spectra was confirmed in both systems, and surface deposits were not found in this experimental condition. There is clear evidence that the changes in peak profile found in the O 1s spectra of the $\text{Li}_x\text{Co}_{0.13}\text{Ni}_{0.13}\text{Mn}_{0.54}\text{O}_{2-\delta}$ electrodes are closely related to the oxygen removal process from the Li_2MnO_3 component at the voltage plateau.

From the Mn 2p, O 1s, and C 1s XPS spectra, the findings are summarized as follows. The oxygen-containing species were accumulated on the electrode surface during discharge below 3.0 V, and then the deposits were decomposed in the second charge process above 4.0 V. These formations/decompositions of the deposits are in good agreement with the voltage plateau observed at the lower current density (Figure 1b and c), suggesting that these processes were accomplished by the electrochemical reactions. In conclusion, it is first proposed that an oxygen molecule, released from the lattice during the initial charge at voltage plateau, is electrochemically reduced at the electrode surface. The oxygen reduction reaction increases the discharge capacity of the Li-excess manganese layered oxides below 3 V. It is also considered that over capacity observed for $\text{Li}_x\text{Co}_{0.13}\text{Ni}_{0.13}\text{Mn}_{0.54}\text{O}_{2-\delta}$ at 60 °C (Figure 1b) is also related to the oxygen reduction reaction.

Surface Analysis by Time-of-Flight Secondary Ion Mass Spectroscopy (TOF-SIMS). XPS analysis revealed that the oxygen molecule was electrochemically reduced and accumulated on the electrode surface. However, its chemistry of the deposits is still unclear. TOF-SIMS analysis, therefore, was conducted to study the chemistry of surface deposits in detail. Figure 5 shows the highlighted TOF-SIMS spectra collected from the electrode surface. The measurements were carried out in a positive-ion

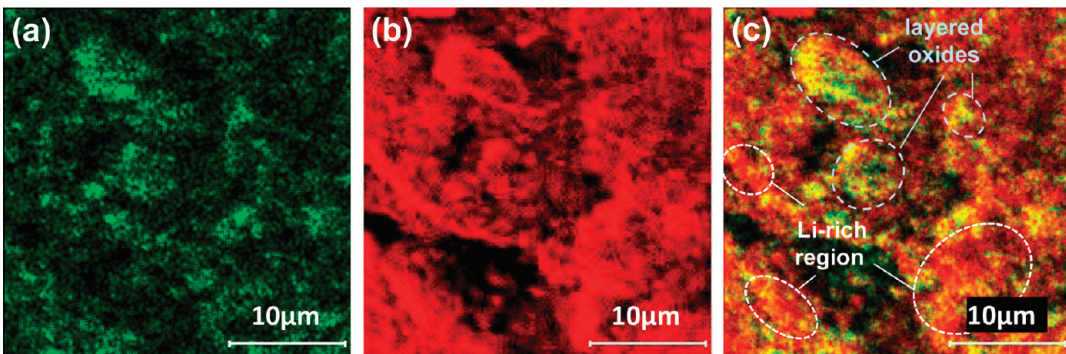


Figure 7. Two-dimensional map obtained by TOF-SIMS from the cycled $\text{Li}_x\text{Ni}_{0.13}\text{Co}_{0.13}\text{Mn}_{0.54}\text{O}_{2-\delta}$ electrode: The distribution of (a) manganese ion and (b) lithium ion in the positive-ion mode. The data were collected from the discharged electrode to 2.0 V after the charging to 4.8 V in 1 M LiPF_6 (EC/DMC). The overlapped image between (a) and (b) is also shown in (c). Manganese and lithium ions are unevenly distributed on the surface of the cycled $\text{Li}_x\text{Ni}_{0.13}\text{Co}_{0.13}\text{Mn}_{0.54}\text{O}_{2-\delta}$ electrode.

mode. The fragments obtained from three different electrodes were compared: (a) initial charge to 4.8 V, (b) discharge to 2.0 V (after the initial charge to 4.8 V), and (c) second charge to 4.8 V. Similar mass spectra are observed on the electrode surface after initial and second charge to 4.8 V. In contrast to the charged electrodes, marked differences are noted in the electrode surface of discharged state: (1) a number of counts at $m/z = 26.98$ (Al^+ fragment) and 27.98 (AlH^+ fragment) are clearly reduced (>10 000 counts for the charged state), and (2) in the discharged state, two signals are observed at $m/z = 30.03$ and 31.04, which can be assigned to Li_2O^+ and LiC_2^+ , respectively. These two fragments disappear after the second charge, and the observed profile in the second charge is very similar to that of the initial charge. It is expected that these two fragments observed in the discharged state originate from the surface deposits as confirmed by the oxygen 1s XPS spectra. It is probable that these fragments are generated from LiO_2 , Li_2O_2 , Li_2O , Li_2CO_3 , etc., which are the possible reduction products of the oxygen molecule.

From TOF-SIMS observation, it is found that these surface deposits consist of not only oxygen, but also lithium and carbon atoms. Note that when the direct electrochemical formation of the $\text{Li}_2\text{O}_2^{51,63}$ with a two-electron reduction process is hypothesized, the signal of LiC_2^+ must not be observed. This fact implies that the surface deposits were partly formed by the different reaction mechanisms including from the electrolyte solution.

Surface Analysis by Synchrotron X-ray Diffraction (SXRD). A careful analysis of the synchrotron XRD shed light on the origin of carbon species detected by TOF-SIMS. The highlighted synchrotron XRD patterns in the 2θ range of $5-11^\circ$ ($5.73-2.60 \text{ \AA}$ in d -spacing) are shown in the insets of Figure 2. The $(1/3\ 1/3\ 0)_{\text{hex}}$ superlattice diffraction line is observed in the pristine sample and the discharged state cycled in the voltage range of 2.0–4.4 V (before the voltage plateau), and this superlattice diffraction line disappears after the charging to 4.8 V (Figure 2c). New diffraction lines at ca. 6.8° , 9.8° , and 10.2° appear after discharge to 2.0 V after charge to 4.8 V beyond the voltage plateau. Moreover, these peaks are not observed after the second charge to 4.8 V.

These three peaks seem to be assigned to the (110) , $(20-2)$, and (002) Bragg diffraction lines of the Li_2CO_3 . The broad (110) diffraction line locating at ca. 6.8° is, however, very close to the position of the $(1/3\ 1/3\ 0)_{\text{hex}}$ diffraction line observed in the as-prepared sample. Therefore, electron diffraction patterns were collected from the same sample to examine whether or not the

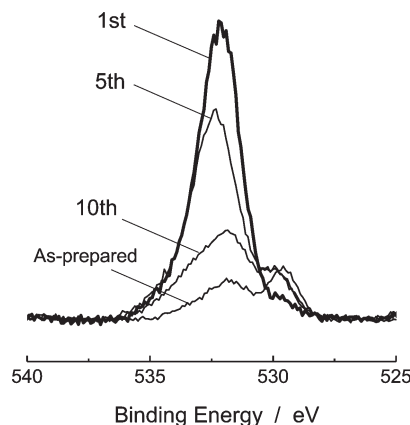


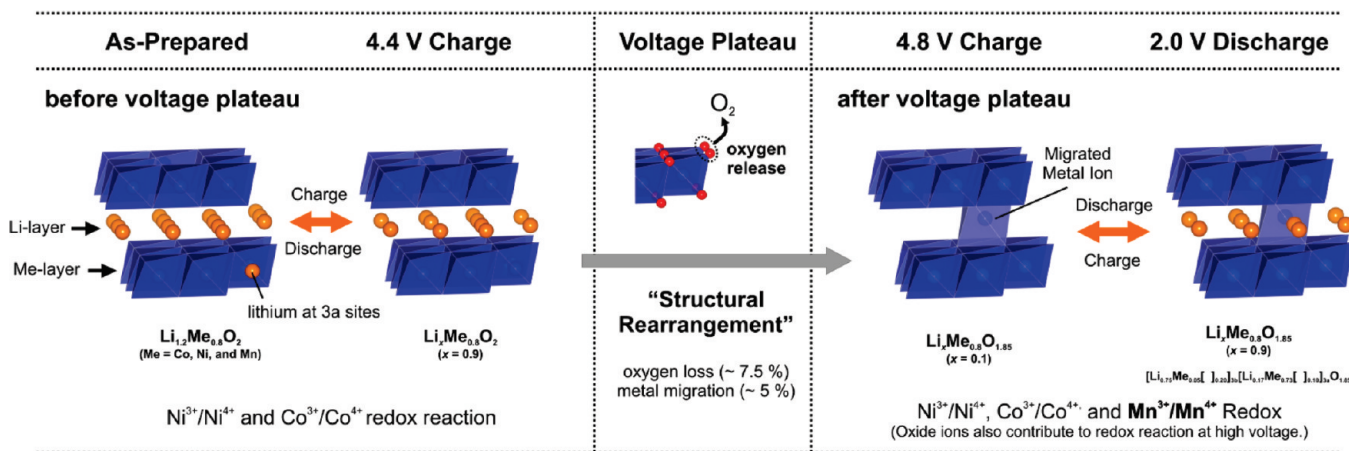
Figure 8. Oxygen 1s XPS spectra collected from the as-prepared and cycled $\text{Li}_x\text{Ni}_{0.13}\text{Co}_{0.13}\text{Mn}_{0.54}\text{O}_{2-\delta}$ electrodes in the voltage range of 2.0–4.8 V in 1 M LiPF_6 (EC/DMC). XPS spectra were collected from the discharged electrodes to 2.0 V after 1, 5, and 10 cycling tests.

broad diffraction line observed in the discharged state originates from the superlattice ordering remaining in the crystal lattice. Typical electron diffraction patterns of the pristine sample and cycled samples (charged to 4.4 or 4.8 V) are shown in Supporting Information Figure S5. A zone-axis was assigned to $[001]_{\text{hex}}$ in all diffraction patterns. The superlattice diffraction spots are not visible by electron diffraction after the charging to 4.8 V.

From these results, it is proved that the broad peak centered at ca. 6.8° is assigned to the (110) diffraction line of Li_2CO_3 , which is one of the products formed by the oxygen reduction reaction. This is consistent with the results of TOF-SIMS, and Li_2CO_3 is responsible for LiC_2^+ fragment observed by TOF-SIMS. In addition to the three peaks assigned to Li_2CO_3 , the broad peak centered at around 8.5° is also noted, which is speculated to be another oxygen reduction product.

Distribution of the Surface Deposits on the Electrode Surface. Distribution on the reaction products formed by the oxygen reduction reaction at the electrode surface was observed by using an optical microscope. Figure 6 shows the optical images of the composite electrodes prepared by discharge to 3.0 or 2.0 V after charging to the voltage plateau. When the images of the as-prepared electrode are compared to the discharged electrode to 3.0 V (no deposits were found by XPS), no apparent change is observed in Figure 6. After further discharging from 3.0 to 2.0 V,

Change in Crystal Structures



Surface Reaction

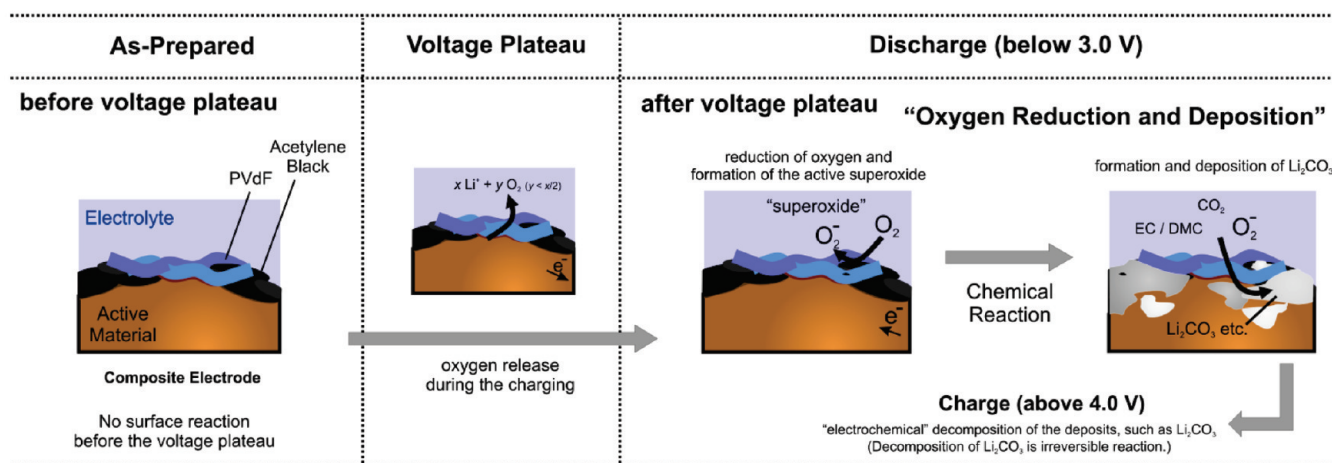


Figure 9. Schemes of the proposed reaction mechanisms in the $\text{Li}_x\text{Ni}_{0.13}\text{Co}_{0.13}\text{Mn}_{0.54}\text{O}_{2-\delta}$ composite electrodes consisting of the active material, acetylene black, and PVdF. Two different mechanisms associated with the bulk particles and surface reactions have been proposed. See the text in detail. A model of the crystal structures was drawn using VESTA.⁷¹

the formation of white particles is obvious on the electrode surface, especially distributing the outer part of electrode surface. The white particles are assigned to be the oxygen reduction products and are found to have a nonuniform particle size (sub-micrometer $\sim 50 \mu\text{m}$), which are distributed on the electrode after the discharging to 2.0 V.

The distribution of chemical species on the electrode was further analyzed by TOF-SIMS, which provides a two-dimensional surface map with a much higher resolution (\sim sub-micrometer size) in comparison to that of the optical microscope. A two-dimensional map was obtained by TOF-SIMS from the discharged electrode to 2.0 V. Signal counts of lithium ($m/z = 6$) are compared to that of manganese ($m/z = 55$) in the positive ion mode in Figure 7. An overlapped image between the Li and Mn ions is shown in Figure 7c. The contrast between Li and Mn must be uniform when the lithium originates from the oxides. The two-dimensional map collected from the as-prepared $\text{Li}_{1.2}\text{Co}_{0.13}\text{Ni}_{0.13}\text{Mn}_{0.54}\text{O}_2$ electrode is also shown in Supporting Information Figure S6. Uniform contrast between Li and Mn is confirmed in

Figure S6, indicating that the source of the lithium ion compares with the manganese ions; this is due to $\text{Li}_{1.2}\text{Ni}_{0.13}\text{Co}_{0.13}\text{Mn}_{0.54}\text{O}_2$ oxide particles. In contrast to the as-prepared electrode, the overlapped image of the discharged sample clearly demonstrates that the source of lithium is not limited to the oxide particles. The oxide particles were partially covered with the lithium-containing deposits, leading to the nonuniformity in the micrometer scale. Note that some oxides were not covered with the deposits at the electrode surface, suggesting that the nucleation rate of the oxygen reduction products (one of them must be Li_2CO_3) is relatively slow in comparison to the growth rate. This leads to the larger size ($\sim 50 \mu\text{m}$) for some deposits as shown in Figure 6c and d.

Reaction Mechanism at the Electrode/Electrolyte Interface. From the results obtained from XPS, TOF-SIMS, and SXRD, we proposed that the oxygen molecule generated at the voltage plateau in the initial cycle is electrochemically reduced below 3.0 V in the discharge process. When we assume the two electron reduction of the oxygen, formation of Li_2O_2 is expected. In this study, the formation of Li_2CO_3 was experimentally

confirmed by SXRD and TOF-SIMS. Therefore, questions arise about the source of carbon in Li_2CO_3 as the product of oxygen reduction and its electrochemical reversibility.

To address these questions related to the Li_2CO_3 , the electrochemical reactivities of the Li_2O_2 and Li_2CO_3 electrodes in the closed cells were compared, and the results are shown in Supporting Information Figure S7. Li_2O_2 can be decomposed by electrochemical oxidation above 4.0 V as already reported by Bruce and co-workers.⁵¹ As shown in Figure S7, Li_2CO_3 is also electrochemically decomposed with a voltage plateau at ca. 4.2 V under the existence of a catalyst, which is 0.2 V higher than that of Li_2O_2 . Charging (oxidation) capacity more than 1000 mAh g⁻¹ is obtained from both materials. XRD shows that the Bragg diffraction lines of Li_2CO_3 completely disappeared after the charging to 4.8 V (Supporting Information Figure S8), indicating that electrochemical decomposition of Li_2CO_3 is possible. This is a consistent result with that Li_2CO_3 on the electrode surface was electrochemically decomposed by the second charge as observed by XPS, TOF-SIMS, and SXRD.

In the discharge cycle, the Li_2O_2 cell shows large discharge capacity (>500 mAh g⁻¹), suggesting that the oxygen molecules, which were released by the electrochemical decomposition of Li_2O_2 upon charging, were electrochemically reduced upon discharging. In contrast to Li_2O_2 , discharge capacity was not observed for Li_2CO_3 . Li_2CO_3 can be decomposed by the electrochemical oxidation, but Li_2CO_3 cannot be reversibly formed by electrochemical reduction. Oxygen molecules were indeed not detected by GC-MS from the gas component of decomposition products in the Li_2CO_3 cell (a laminate-type cell was used in this test). These observations suggest that Li_2CO_3 can form as a byproduct of the oxygen reduction reaction. Oxygen is electrochemically reduced with one electron reduction process in the ionic liquid media, forming a superoxide.⁶⁴ The superoxide is stable in the ionic liquid, but may not be stable in carbonate-based electrolyte solution (EC/DMC) used in this study. This reaction might be facilitated by the oxide and carbon as the catalyst. The superoxide ion could further react with the carbonate-based electrolyte solution and/or its decomposed products, for example, carbon monoxide/dioxide. Acetylene black in the composite electrode could be also another possibility as carbon source of Li_2CO_3 . Recently, oxygen reduction/oxidation reactions in the aprotic electrolyte solution have been examined by several research groups for Li-Air batteries applications. Although the reversibility of the oxygen electrode is significantly improved by the electrocatalysts,^{65–67} the electrolyte solution and salts are also important factors.^{68,69} Li_2CO_3 and lithium alkyl carbonate were also found as the reduction products by FT-IR,⁷⁰ which is consistent with that of our observations.

From these results, it is hypothesized that the reversible capacity of the surface redox reaction is lost in subsequent cycles once Li_2CO_3 formed at the electrode surface. To test this hypothesis, XPS spectra of the electrodes were collected after cycling tests. Figure 8 shows the change in the O 1s XPS spectra of the cycled electrode after the first, fifth, and 10th cycles (discharged to 2.0 V). As shown in Figure 8, the intensity of O 1s XPS spectra was reduced as a function of the cycle number, indicating that the deposits as the reaction products of oxygen reduction have been lost from the electrode surface in this experimental condition. This is probably consistent with the fact that the voltage plateau at 2.5 V for the discharge is not observed after five cycles, indicating that the discharge capacity of the Li-excess manganese layered materials is

mainly obtained by the conventional lithium insertion/extraction process into/from the oxide particles after several cycles.

In conclusion, the charge/discharge capacity, which originated from the redox reaction of oxygen molecule at the electrode surface, declined rapidly when the formation of Li_2CO_3 is confirmed. The proposed reaction mechanism can be extended to similar Li-excess manganese layered oxides and rechargeable Li-air batteries.^{51,63} In Li-air batteries, the supply of oxygen is unlimited, but the depletion of electrolyte must be considered. Therefore, it is believed that reversibility of the surface redox reaction of oxygen is improved by the suppression of the Li_2CO_3 formation with the optimization of the electrolyte solution.

CONCLUSIONS

The reaction mechanisms of $\text{Li}_{1.2}\text{Co}_{0.13}\text{Ni}_{0.13}\text{Mn}_{0.54}\text{O}_2$ as an electrode material for rechargeable batteries have been examined by SXRD, XAS, TOF-SIMS, and XPS. On the basis of these results, it is proposed that high capacity of the Li-excess manganese layered oxides after the first charge to the high voltage is divided into two mechanisms: one is the activated manganese redox reaction ($\text{Mn}^{3+}/\text{Mn}^{4+}$), and another is the oxygen reduction reaction at the electrode surface. The proposed reaction schemes are summarized in Figure 9. The reversible solid-state redox reaction occurs in the range of 2.0–4.4 V. During the charge to 4.8 V beyond the high voltage plateau, lithium and oxide ions are simultaneously extracted from the oxide particles. Rietveld analysis reveals that approximately 7.5% of oxide ion is removed from the lattice at the voltage plateau, which is lower than the amount of the oxide ion removed from the lattice calculated on the basis of Li_2O removal. Both SXRD data and the simulation of the XANES spectra at Ni K-edge indicate that this process is accompanied by the cation rearrangement process including the nickel migration process from metal to lithium layer (~5%). The XAS analysis suggested that tetravalent manganese ions in the pristine sample are partially reduced to the trivalent state in discharge because of the reconstruction of the Fermi level after the oxide ion removal process. Because the results are consistent with that of other Li-excess manganese layered systems, these structural modification processes in the bulk particles are regarded as the common characteristics in this system.

This Article has addressed the question related to the role of oxygen molecules released at the high voltage plateau in the discharge process and has demonstrated that oxygen is electrochemically reduced at the electrode surface in the discharge process below 3 V. Electrochemical reduction of the oxygen molecule resulted in the deposition on the electrode surface, specifically on the carbon and oxides. Lithium carbonate is found as the one of the major components of the reaction products, which is the byproduct of the oxygen reduction reaction. The electrochemically active oxygen is consumed by the formation of Li_2CO_3 , and then the reversible capacity related to the surface redox reaction declines. It was concluded that suppression of the lithium carbonate formation is necessary to improve the cyclability of the surface redox reaction. It is believed that improvement of the reversibility of the oxygen redox reaction at the electrode surface will result in the development of the new high-capacity positive electrode materials using both conventional solid-state redox reaction and reversible redox reactions at the electrode surface in the closed system.

■ ASSOCIATED CONTENT

S Supporting Information. Rietveld analysis of the cycled $\text{Li}_x\text{Ni}_{0.13}\text{Co}_{0.13}\text{Mn}_{0.54}\text{O}_{2-\delta}$ with different restrictions, schematic illustrations of the different local environments for the tetravalent nickel ions used for the XANES simulation by FEFF, oxygen 1s XPS spectra obtained from the cycled $\text{LiNi}_{0.13}\text{Co}_{0.13}\text{Mn}_{0.54}\text{O}_2$ and $\text{LiCo}_{1/3}\text{Ni}_{1/3}\text{Mn}_{1/3}\text{O}_2$ electrode, electron diffraction patterns of the cycled $\text{Li}_x\text{Ni}_{0.13}\text{Co}_{0.13}\text{Mn}_{0.54}\text{O}_{2-\delta}$ particles, two-dimensional map of as-prepared $\text{LiNi}_{0.13}\text{Co}_{0.13}\text{Mn}_{0.54}\text{O}_2$ electrode obtained by TOF-SIMS, first charge/discharge curves of the $\text{Li}/\text{Li}_2\text{CO}_3$ and $\text{Li}/\text{Li}_2\text{O}_2$ cells, and XRD patterns of the cycled Li_2CO_3 electrodes. This material is available free of charge via the Internet at <http://pubs.acs.org>.

■ AUTHOR INFORMATION

Corresponding Author

komaba@rs.kagu.tus.ac.jp

■ ACKNOWLEDGMENT

This work was financially supported in part by NEDO and KAKENHI (No. 21750194). The synchrotron X-ray diffraction experiments were made possible through the support of the Japanese Ministry of Education, Science, Sports and Culture, Nanotechnology Support Project (Proposal No. 2009B1777/BL02B2), with the approval of Japan Synchrotron Radiation Research Institute (JASRI). The synchrotron X-ray absorption work was done under the approval of the Photon Factory Program Advisory Committee (Proposal Nos. 2008G58, 2008G615, and 2009G627). We thank Mr. Abe, graduate student at Tokyo University of Science in Japan, for helping with the experimental works in the Photon Factory. We are grateful to Mr. Ishizhima and Dr. Iida from ULVAC-PHI Inc. for the two-dimensional TOF-SIMS mapping of the samples. We thank Assoc. Prof. Koyama at Kyoto University in Japan for fruitful discussions.

■ REFERENCES

- (1) Ohzuku, T.; Kitagawa, M.; Hirai, T. *J. Electrochem. Soc.* **1990**, *137*, 769.
- (2) Tarascon, J. M.; McKinnon, W. R.; Coowar, F.; Bowmer, T. N.; Amatucci, G.; Guyomard, D. *J. Electrochem. Soc.* **1994**, *141*, 1421.
- (3) Thackeray, M. M.; Shao-Horn, Y.; Kahajan, A. J.; Kepler, K. D.; Vaughey, J. T.; Hackney, S. A. *Electrochem. Solid-State Lett.* **1998**, *1*, 7.
- (4) Paulsen, J. M.; Dahn, J. R. *Chem. Mater.* **1999**, *11*, 3065.
- (5) Kang, S. H.; Goodenough, J. B.; Rabenberg, L. K. *Chem. Mater.* **2001**, *13*, 1758.
- (6) Piszora, P.; Nowicki, W.; Darul, J.; Bojanowski, B.; Carlson, S.; Cerenius, Y. *Radiat. Phys. Chem.* **2009**, *78*, S89.
- (7) Komaba, S.; Yabuuchi, N.; Ikemoto, S. *J. Solid State Chem.* **2010**, *183*, 234.
- (8) Padhi, A. K.; Nanjundaswamy, K. S.; Goodenough, J. B. *J. Electrochem. Soc.* **1997**, *144*, 1188.
- (9) Andersson, A. S.; Kalska, B.; Haggstrom, L.; Thomas, J. O. *Solid State Ionics* **2000**, *130*, 41.
- (10) Yamada, A.; Chung, S. C.; Hinokuma, K. *J. Electrochem. Soc.* **2001**, *148*, A224.
- (11) Johnson, C. S.; Kim, J. S.; Lefief, C.; Li, N.; Vaughey, J. T.; Thackeray, M. M. *Electrochem. Commun.* **2004**, *6*, 1085.
- (12) Thackeray, M. M.; Johnson, C. S.; Vaughey, J. T.; Li, N.; Hackney, S. A. *J. Mater. Chem.* **2005**, *15*, 2257.
- (13) Thackeray, M. M.; Kang, S. H.; Johnson, C. S.; Vaughey, J. T.; Hackney, S. A. *Electrochem. Commun.* **2006**, *8*, 1531.
- (14) Johnson, C. S.; Li, N. C.; Lefief, C.; Vaughey, J. T.; Thackeray, M. M. *Chem. Mater.* **2008**, *20*, 6095.
- (15) Numata, K.; Sakaki, C.; Yamanaka, S. *Solid State Ionics* **1999**, *117*, 257.
- (16) Ammundsen, B.; Paulsen, J.; Davidson, I.; Liu, R. S.; Shen, C. H.; Chen, J. M.; Jang, L. Y.; Lee, J. F. *J. Electrochem. Soc.* **2002**, *149*, A431.
- (17) Lu, Z. H.; MacNeil, D. D.; Dahn, J. R. *Electrochem. Solid-State Lett.* **2001**, *4*, A191.
- (18) Lu, Z. H.; Dahn, J. R. *J. Electrochem. Soc.* **2002**, *149*, A815.
- (19) Lu, Z. H.; Beaulieu, L. Y.; Donaberger, R. A.; Thomas, C. L.; Dahn, J. R. *J. Electrochem. Soc.* **2002**, *149*, A778.
- (20) Grey, C. P.; Yoon, W. S.; Reed, J.; Ceder, G. *Electrochem. Solid-State Lett.* **2004**, *7*, A290.
- (21) Guo, X. J.; Li, Y. X.; Zheng, M.; Zheng, J. M.; Li, J.; Gong, Z. L.; Yang, Y. *J. Power Sources* **2008**, *184*, 414.
- (22) Jiang, M.; Key, B.; Meng, Y. S.; Grey, C. P. *Chem. Mater.* **2009**, *21*, 2733.
- (23) Lim, J. H.; Bang, H.; Lee, K. S.; Amine, K.; Sun, Y. K. *J. Power Sources* **2009**, *189*, 571.
- (24) Meng, Y. S.; Ceder, G.; Grey, C. P.; Yoon, W. S.; Jiang, M.; Breger, J.; Shao-Horn, Y. *Chem. Mater.* **2005**, *17*, 2386.
- (25) Tabuchi, M.; Nabeshima, Y.; Shikano, M.; Ado, K.; Kageyama, H.; Tatsumi, K. *J. Electrochem. Soc.* **2007**, *154*, A638.
- (26) Wang, Q. Y.; Liu, J.; Murugan, A. V.; Manthiram, A. *J. Mater. Chem.* **2009**, *19*, 4965.
- (27) Wu, Y.; Murugan, A. V.; Manthiram, A. *J. Electrochem. Soc.* **2008**, *155*, A635.
- (28) Zhang, L. Q.; Takada, K.; Ohta, N.; Fukuda, K.; Osada, M.; Wang, L. Z.; Sasaki, T.; Watanabe, M. *J. Electrochem. Soc.* **2005**, *152*, A171.
- (29) van Bommel, A.; Dahn, J. R. *Electrochem. Solid-State Lett.* **2010**, *13*, A62.
- (30) Kalyani, P.; Chitra, S.; Mohan, T.; Gopukumar, S. *J. Power Sources* **1999**, *80*, 103.
- (31) Robertson, A. D.; Bruce, P. G. *Chem. Commun.* **2002**, 2790.
- (32) Robertson, A. D.; Bruce, P. G. *Chem. Mater.* **2003**, *15*, 1984.
- (33) Gan, C. L.; Zhan, H.; Hu, X. H.; Zhou, Y. H. *Electrochem. Commun.* **2005**, *7*, 1318.
- (34) Yu, D. Y. W.; Yanagida, K.; Kato, Y.; Nakamura, H. *J. Electrochem. Soc.* **2009**, *156*, A417.
- (35) Tran, N.; Croguennec, L.; Menetrier, M.; Weill, F.; Biensan, P.; Jordy, C.; Delmas, C. *Chem. Mater.* **2008**, *20*, 4815.
- (36) Armstrong, A. R.; Holzapfel, M.; Novak, P.; Johnson, C. S.; Kang, S. H.; Thackeray, M. M.; Bruce, P. G. *J. Am. Chem. Soc.* **2006**, *128*, 8694.
- (37) Verdier, S.; El Ouatani, L.; Dedryvere, R.; Bonhomme, F.; Biensan, P.; Gonbeau, D. *J. Electrochem. Soc.* **2007**, *154*, A1088.
- (38) Dedryvere, R.; Maccario, M.; Croguennec, L.; Le Cras, F.; Delmas, C.; Gonbeau, D. *Chem. Mater.* **2008**, *20*, 7164.
- (39) Talyosef, Y.; Markovsky, B.; Salitra, G.; Aurbach, D.; Kim, H. J.; Choi, S. *J. Power Sources* **2005**, *146*, 664.
- (40) Lu, Y. C.; Mansour, A. N.; Yabuuchi, N.; Shao-Horn, Y. *Chem. Mater.* **2009**, *21*, 4408.
- (41) Adriaens, A.; Van Vaeck, L.; Adams, F. *Mass Spectrom. Rev.* **1999**, *18*, 48.
- (42) Van Vaeck, L.; Adriaens, A.; Gijbels, R. *Mass Spectrom. Rev.* **1999**, *18*, 1.
- (43) Koyama, Y.; Yabuuchi, N.; Tanaka, I.; Adachi, H.; Ohzuku, T. *J. Electrochem. Soc.* **2004**, *151*, A1545.
- (44) Yabuuchi, N.; Koyama, Y.; Nakayama, N.; Ohzuku, T. *J. Electrochem. Soc.* **2005**, *152*, A1434.
- (45) Yabuuchi, N.; Makimura, Y.; Ohzuku, T. *J. Electrochem. Soc.* **2007**, *154*, A314.
- (46) Zheng, J. M.; Zhang, Z. R.; Wu, X. B.; Dong, Z. X.; Zhu, Z.; Yang, Y. *J. Electrochem. Soc.* **2008**, *155*, A775.
- (47) Nishibori, E.; Takata, M.; Kato, K.; Sakata, M.; Kubota, Y.; Aoyagi, S.; Kuroiwa, Y.; Yamakata, M.; Ikeda, N. *Nucl. Instrum. Methods Phys. Res., Sect. A* **2001**, *467*, 1045.

- (48) Izumi, F.; Ikeda, T. In *European Powder Diffraction, Pts 1 and 2*; Delhez, R., Mittemeijer, E. J., Eds.; Trans Tech Publications Ltd.: Zurich-Uetikon, 2000; Vol. 321-3, p 198.
- (49) Newville, M. *J. Synchrot. Radiat.* **2001**, 8, 322.
- (50) Rehr, J. J.; Albers, R. C. *Rev. Mod. Phys.* **2000**, 72, 621.
- (51) Ogasawara, T.; Debart, A.; Holzapfel, M.; Novak, P.; Bruce, P. G. *J. Am. Chem. Soc.* **2006**, 128, 1390.
- (52) Breger, J.; Jiang, M.; Dupre, N.; Meng, Y. S.; Shao-Horn, Y.; Ceder, G.; Grey, C. P. *J. Solid State Chem.* **2005**, 178, 2575.
- (53) Boulineau, A.; Croguennec, L.; Delmas, C.; Weill, F. *Chem. Mater.* **2009**, 21, 4216.
- (54) Yabuuchi, N.; Kumar, S.; Li, H. H.; Kim, Y. T.; Shao-Horn, Y. *J. Electrochem. Soc.* **2007**, 154, A566.
- (55) Yabuuchi, N.; Kim, Y. T.; Li, H. H.; Shao-Horn, Y. *Chem. Mater.* **2008**, 20, 4936.
- (56) Breger, J.; Meng, Y. S.; Hinuma, Y.; Kumar, S.; Kang, K.; Shao-Horn, Y.; Ceder, G.; Grey, C. P. *Chem. Mater.* **2006**, 18, 4768.
- (57) Myung, S. T.; Komaba, S.; Kurihara, K.; Hosoya, K.; Kumagai, N.; Sun, Y. K.; Nakai, I.; Yonemura, M.; Kamiyama, T. *Chem. Mater.* **2006**, 18, 1658.
- (58) Kang, S. H.; Park, S. H.; Johnson, C. S.; Amine, K. *J. Electrochem. Soc.* **2007**, 154, A268.
- (59) Tang, P.; Holzwarth, N. A. W. *Phys. Rev. B* **2003**, 68, 165107.
- (60) Koyama, Y.; Tanaka, I.; Nagao, M.; Kanno, R. *J. Power Sources* **2009**, 189, 798.
- (61) Yoon, W. S.; Balasubramanian, M.; Chung, K. Y.; Yang, X. Q.; McBreen, J.; Grey, C. P.; Fischer, D. A. *J. Am. Chem. Soc.* **2005**, 127, 17479.
- (62) Treuil, N.; Labrugere, C.; Menetrier, M.; Portier, J.; Campet, G.; Deshayes, A.; Frison, J. C.; Hwang, S. J.; Song, S. W.; Choy, J. H. *J. Phys. Chem. B* **1999**, 103, 2100.
- (63) Abraham, K. M.; Jiang, Z. *J. Electrochem. Soc.* **1996**, 143, 1.
- (64) Katayama, Y.; Sekiguchi, K.; Yamagata, M.; Miura, T. *J. Electrochem. Soc.* **2005**, 152, E247.
- (65) Debart, A.; Paterson, A. J.; Bao, J.; Bruce, P. G. *Angew. Chem., Int. Ed.* **2008**, 47, 4521.
- (66) Giordani, V.; Freunberger, S. A.; Bruce, P. G.; Tarascon, J. M.; Larcher, D. *Electrochem. Solid-State Lett.* **2010**, 13, A180.
- (67) Lu, Y. C.; Xu, Z. C.; Gasteiger, H. A.; Chen, S.; Hamad-Schifferli, K.; Shao-Horn, Y. *J. Am. Chem. Soc.* **2010**, 132, 12170.
- (68) Laoire, C. O.; Mukerjee, S.; Abraham, K. M.; Plichta, E. J.; Hendrickson, M. A. *J. Phys. Chem. C* **2009**, 113, 20127.
- (69) Laoire, C. O.; Mukerjee, S.; Abraham, K. M.; Plichta, E. J.; Hendrickson, M. A. *J. Phys. Chem. C* **2010**, 114, 9178.
- (70) Mizuno, F.; Nakanishi, S.; Kotani, Y.; Yokoishi, S.; Iba, H. *Electrochemistry* **2010**, 78, 403.
- (71) Momma, K.; Izumi, F. *J. Appl. Crystallogr.* **2008**, 41, 653.